iScience

CellPress
OPEN ACCESS

Article

Converting Immune Cold into Hot by Biosynthetic Functional Vesicles to Boost Systematic Antitumor Immunity

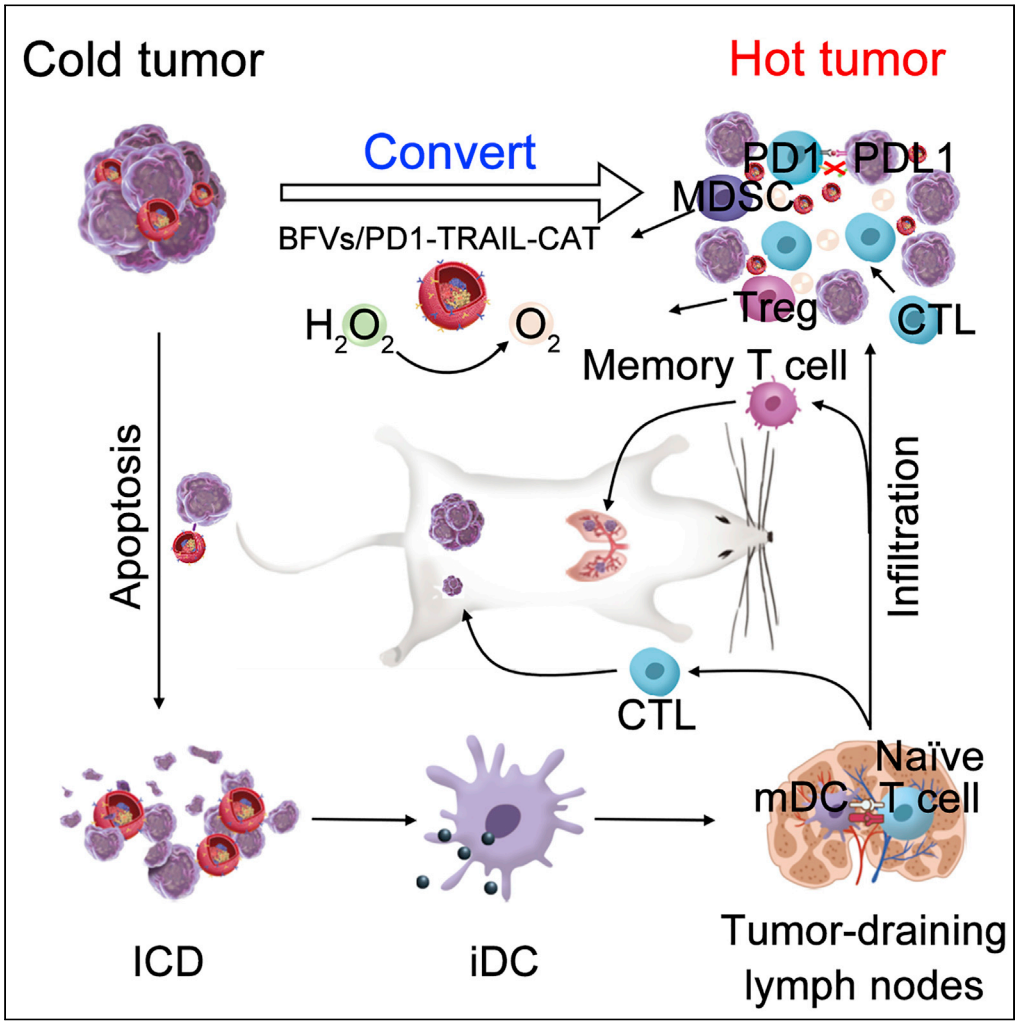

Ming Wu, Dongye Zheng, Da Zhang, ..., Xinyi Lin, Jingfeng Liu, Xiaolong Liu

drjingfeng@126.com (J.L.)
xiaoloong.liu@gmail.com (X.L.)

HIGHLIGHTS

BFVs integrated PD1, TRAIL, and Catalase to convert immune cold tumor into hot

TRAIL induces cancer cell immunogenic death, ectogenic PD1 blocks checkpoint signal

Catalase reduces TME hypoxia to enhance effector T cell infiltration and activation

BFVs boost systematic antitumor immunity and achieve long-term immune memory

Wu et al., iScience 23, 101341
July 24, 2020
https://doi.org/10.1016/j.isci.2020.101341

iScience

CellPress
OPEN ACCESS

Article

Converting Immune Cold into Hot by Biosynthetic Functional Vesicles to Boost Systematic Antitumor Immunity

Ming Wu,[1,2,3,6] Dongye Zheng,[1,2,6] Da Zhang,[1,3,6] Peiwen Yu,[1,3] Lianli Peng,[4] Feng Chen,[1,2] Ziguo Lin,[1] Zhixiong Cai,[1,3] Jiong Li,[1] Zuwu Wei,[1,3] Xinyi Lin,[1,3] Jingfeng Liu,[1,2,3,5,*] and Xiaolong Liu[1,2,3,5,7,*]

SUMMARY

Immune cold tumor characterized by low immunogenicity, insufficient and exhausted tumor-infiltrating lymphocytes, and immunosuppressive microenvironment is the main bottleneck responsible for low patient response rate of immune checkpoint blockade. Here, we developed biosynthetic functional vesicles (BFVs) to convert immune cold into hot through overcoming hypoxia, inducing immunogenic cell death, and immune checkpoint inhibition. The BFVs present PD1 and tumor necrosis factor-related apoptosis-inducing ligand (TRAIL) on the surface, whereas load catalase into their inner core. The TRAIL can specifically induce immunogenic death of cancer cells to initiate immune response, which is further synergistically strengthened by blocking PD1/PDL1 checkpoint signal through ectogenic PD1 proteins on BFVs. The catalase can produce O_2 to overcome tumor hypoxia, in turn to increase infiltration of effector T cells while deplete immunosuppressive cells in tumor. The BFVs elicit robust and systematic antitumor immunity, as demonstrated by significant regression of tumor growth, prevention of abscopal tumors, and excellent inhibition of lung metastasis.

INTRODUCTION

Immune checkpoint blockade (ICB) therapy has shown great therapeutic potential in various cancer types, including melanoma, renal carcinoma, head and neck squamous cell carcinomas, non-small cell lung cancer, urothelial carcinoma, and bladder cancer (Tang et al., 2018; Tumeh et al., 2014). In particular, ICB therapy by monoclonal antibodies specific for the immune checkpoint proteins of programmed cell death receptor-1 (PD1) or its predominant ligand (PDL1) has achieved tremendous success in clinic (Boussiotis, 2016; Zou et al., 2016). However, only a small portion of patients benefit from current ICB therapies (Robert et al., 2015; Topalian et al., 2012), mainly ascribed to many tumors inherently featured as immune cold with low level and exhausted tumor-infiltrating lymphocytes (TILs), insufficient tumor antigen burden, and immunosuppressive microenvironment caused by tumor hypoxia, which does not respond well to ICB therapies (Galon and Bruni, 2019; Huang et al., 2019). Although combination of ICB with various other therapeutic modalities (i.e., radiotherapy [Chao et al., 2018], chemotherapy [Wang et al., 2018], phototherapy [He et al., 2016], and other immunotherapies [Wolchok et al., 2013]) has achieved a synergistic effect to some degree, the clinical outcome is still not satisfactory as these therapeutic modalities are also very difficult to convert immune cold into hot as well as they have their own intrinsic defects, such as radiation of radiotherapy, severe systemic toxicity of chemotherapy, shallow tissue penetration of phototherapy and serious cumulative immune-related toxicities of combinational immunotherapies, all of which inevitably hinder their further clinical efficacy (Yue et al., 2019). Therefore, more rational synergistic approaches that can robustly convert the immune cold tumor into hot are extremely on demand to improve the therapeutic potential of ICB.

Up to now, several strategies have been developed to amplify immunomodulatory effects (Chen et al., 2019; Chiang et al., 2018; Galstyan et al., 2019; Mi et al., 2018; Ruan et al., 2019; Wang et al., 2016, 2019). Among them, biosynthetic functional vesicles (BFVs) with surface presenting PD1 proteins hold great promise to improve cancer immunotherapy efficiency, owing to their unique advantages including excellent biocompatibility and high fidelity of surface markers (Liu et al., 2019; Zhang et al., 2018a, 2018b, 2018c). However, other typical immunosuppressive features involved in immune cold tumor, for example, low

[1]The United Innovation of Mengchao Hepatobiliary Technology Key Laboratory of Fujian Province, Mengchao Hepatobiliary Hospital of Fujian Medical University, Fuzhou 350025, P. R. China

[2]CAS Key Laboratory of Design and Assembly of Functional Nanostructures, Fujian Institute of Research on the Structure of Matter, Chinese Academy of Sciences, Fuzhou 350002, P. R. China

[3]Mengchao Med-X Center, Fuzhou University, Fuzhou 350116, P. R. China

[4]College of Engineering and Computer Science, The Australian National University, Canberra 2601, Australia

[5]Department of Translational Medicine, Xiamen Institute of Rare Earth Materials, Chinese Academy of Sciences, Xiamen 361024, P. R. China

[6]These authors contributed equally

[7]Lead Contact

*Correspondence: drjingfeng@126.com (J.L.), xiaoloong.liu@gmail.com (X.L.)

https://doi.org/10.1016/j.isci.2020.101341

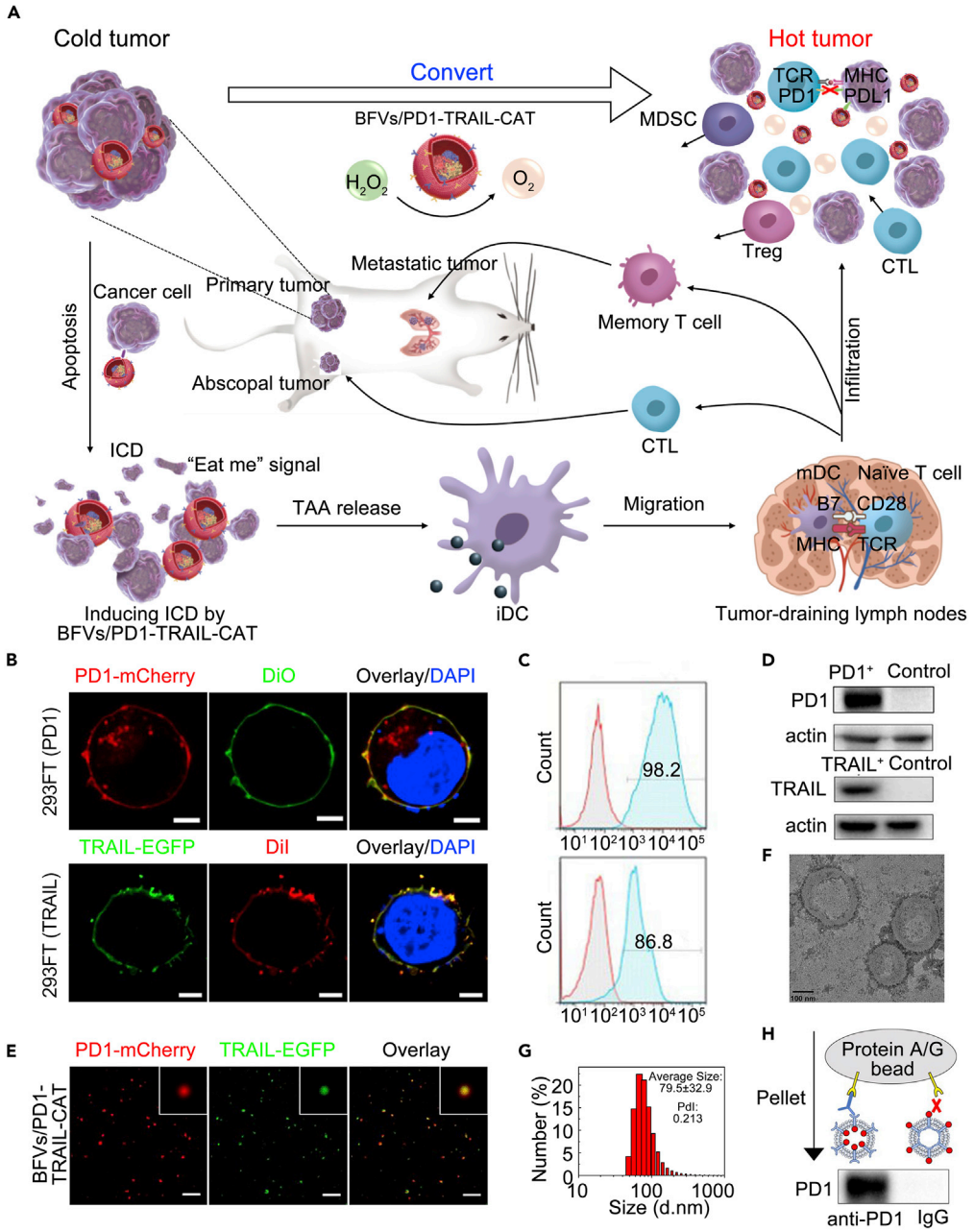

Figure 1. BFVs Synergistically Improve Immunotherapy by Converting Immune Cold into Hot

(A) Schematic illustration of the mechanism of BFVs to generate robust antitumor immune responses. TRAIL can specifically induce immunogenic cancer cell death (ICD) to initiate immune responses. Ectogenic PD1 proteins on BFVs can block the PD-1/PDL1 immune checkpoint to further synergistically strengthen the immune responses. CAT can alleviate tumor hypoxia to enhance intra-tumoral infiltration of effector T cells and weaken immunosuppression.

(B) Confocal images of HEK293 FT cells stably expressing mouse PD1 and mouse TRAIL on cell membranes, respectively. DiO and DiI were used to stain cell membrane (scale bar: 10 μm).

(C) The representative flow cytometric analysis of PD1-expressing (gated on mCherry^{+}) and TRAIL-expressing (gated on EGFP^{+}) HEK293 FT stable cells.

(D) Western blot assay to confirm the expression of mouse PD1 (indicated as PD1^{+}) and mouse TRAIL (indicated as TRAIL^{+}) in 293FT cells. Actin was used as the loading control.

(E) Confocal images to demonstrate the co-existence of PD1-mCherry and TRAIL-EGFP on the single vesicle by the overlap of red/green fluorescence (scale bar: 10 μm).

(F) The transmission electron microscopy image of BFVs (scale bar: 50 nm).

Figure 1. *Continued*
(G) The size distribution of BFVs through dynamic light scattering analysis.
(H) Coimmunoprecipitation (coIP) and western blot to examine the right outside-out orientation of PD1 on the BFVs. Anti-PD1 antibody could pull down BFVs, whereas IgG as a control could not bind to PD1 proteins on BFVs.

tumor associated antigen (TAA) burden that inhibits the recognition ability or activation of cytotoxic T cells in tumor, still extensively exist to significantly impair the immunotherapy effect. Thus, in addition to PDL1 blockade, the BFVs that can simultaneously induce immunogenic cell death (ICD) of cancer cells to increase tumor immunogenicity (such as TAA burden) are extremely needed to improve the ICB efficacy. Tumor necrosis factor-related apoptosis-inducing ligand (TRAIL) is a promising biotherapeutic candidate that can specifically induce apoptosis of cancer cells without causing toxicity to normal cells (von Karstedt et al., 2017). Therefore, TRAIL might be a potential ICD inducer and could seamlessly cooperate with ectogenic PD1 when both of them are presented on BFVs.

Although the cooperation of TRAIL and PD1 can synergistically improve the tumor immunogenicity, the dynamic immune evasion mechanisms due to the complicated tumor microenvironment (TME) of solid cold tumor still often lead to therapeutic failure (Binnewies et al., 2018; Kim et al., 2018). Typically, solid tumors are characterized by a highly hypoxic TME, which contributes to immune resistance and immune suppression/tolerance through multi-pathways, including recruitment of immunosuppressive cells (i.e., myeloid-derived suppressor cells [MDSCs], tumor-associated macrophages [TAMs], and T-regulatory [Treg] cells), making cancer cells resistant to cytotoxic T lymphocyte (CTL)-mediated lysis, desensitization of chemokine receptors, and reduction of proinflammatory cytokines (Noman et al., 2015). Therefore, alleviating the hypoxia of TME would be a powerful strategy to reverse immune cold into hot for improving immunotherapy outcomes. Although respiratory hyperoxia has been applied to decrease the intra-tumoral hypoxia for reinforcing immunotherapy effect (Hatfield et al., 2015), this protocol also produced excessive amounts of reactive O_2 species (ROS) that might overwhelm natural antioxidant defenses to destroy normal cellular structures (e.g., inducing hyperoxic acute lung injury [Kallet and Matthay, 2013]). Compared with such systemic O_2 supply strategy, *in situ* intra-tumoral generation of O_2 will be a more efficient, favorable, and safe approach for alleviating hypoxia but has rarely been reported to modulate the immune responses.

To overcome the low immune responses of ICB therapy in cold tumors, we herein proposed a proof-of-concept strategy by designing BFVs with surface presenting PD1 and TRAIL while encapsulating catalase (CAT) into the inner core to thoroughly convert tumor from immune cold into hot milieu for eliciting robust and systematic antitumor immunity (Figure 1A). We hypothesized that the TRAIL component on BFVs could initiate the immune responses by specifically inducing immunogenic cancer cell death, which could be further strengthened by collaborating with presented ectogenic PD1 proteins as the checkpoint blockade to reactivate the anergic tumor-specific CTLs; in addition, the CAT could catalyze highly abundant H_2O_2 in TME for *in situ* generation of O_2, thus to ameliorate tumor hypoxia for systematically reversing the un-favorable environment of ICB therapy to ensure the trafficking and killing activities of CTLs in tumors. The comprehensive immuno-modulating ability and robust antitumor immunity of our BFVs have been clearly demonstrated in immune cold tumor models (4T1 breast tumor models [Sagiv-Barfi et al., 2015], including both subcutaneous and orthotopic models), through significant primary tumor growth regression, excellent metastasis prevention, obvious distal and immune-memory effects, and long-term survival benefits. Taken together, the here reported BFVs can elicit potent and durable immune responses by turning immune cold tumors into hot, and in principle it might be an universal immunotherapy paradigm for various other solid tumors and very promising for future translation.

RESULTS

Fabrication of BFVs

To bio-synthesize the functional vesicles (as depicted in Figure S1), we first established stable HEK293 FT cells expressing the proteins of mouse PD1 fused with mCherry (PD1-mCherry) and TRAIL fused with EGFP (TRAIL-EGFP) on the cell membrane, respectively, by using lentiviral vector for corresponding gene transfection (Figure S2). As shown in Figure 1B, the PD1 fusing proteins and the TRAIL fusing proteins were nicely expressed on the plasma membrane of transfected cells through confocal laser scanning microcopy (CLSM) observation, evidenced by their co-localization with cell membrane-staining dyes. Flow cytometry analysis further proved that nearly 90% of the genetically engineered cells were PD1 or TRAIL positive

(Figure 1C), and the stable over-expression of the PD1 or TRAIL proteins can be further confirmed by western blot (WB) analysis (Figures 1D, S3A, and S3B). Collectively, these results clearly confirm the successful display of PD1 or TRAIL proteins on the membrane of HEK293 FT cells.

Then, the cell membranes of engineered HEK293 FT cells were extracted, and the BFVs were obtained by co-extrusion of PD1 anchoring membranes, TRAIL anchoring membranes, and commercially available CAT through 1, 0.4, 0.2, and 0.1 μm pore-sized polycarbonate membrane filters. To vividly observe the co-existence of PD1 and TRAIL on BFVs, the rough products extruded through 1-μm filters were imaged by CLSM (Figure 1E). As expected, the vesicles presented both green fluorescence of TRAIL-EGFP and red fluorescence of PD1-mCherry, demonstrating the successful fusion of both cell membranes. Next, the morphology and size of BFVs were characterized by transmission electron microscopy and dynamic light scattering analyses, which showed a uniform vesicular morphology with average diameter around 100 nm (Figures 1F, 1G, S4A and S4B). The zeta potential of the BFVs was determined as -24.9 ± 1.1 mV (Figure S4C). The immunoprecipitation assay showed that the anti-PD1 antibody could pull down the majority of BFVs, demonstrating the PD1 protein had a right outside-out orientation on most of the BFVs (Figures 1H and S3C).

In addition, we fabricated BFVs with larger size by extruding cell membranes (pre-labeled with DiO) and CAT (pre-labeled with Cy5) through 10-μm filters, to intuitively demonstrate the CAT can be encapsulated inside the inner core of BFVs by using CLSM. As shown in Figure S5A, the physical mixture of CAT and cell membranes (without co-extrusion) that exhibited only DiO green fluorescence, implying the free CAT unloaded in BFVs, could be completely removed by repeated washing in the process of producing BFVs. However, BFVs/CAT obtained by co-extrusion of BFVs and CAT showed dual and merged fluorescence signals, demonstrating the co-existence of cell membranes and CAT. Furthermore, 3D reconstruction of z stack images (Figure S5A) and plot profile (Figure S5B) along a single merged fluorescence vesicle revealed that the CAT was successfully encapsulated inside the BFV. Furthermore, we also compared the enzyme activity of the final product from physical mixing or from the co-extrusion procedure through detecting the H_2O_2 scavenge ability by using $TiOSO_4$ as a color probe (from colorless to yellow after encountering H_2O_2 with maximum absorbance at 450 nm), to verify the encapsulation of CAT inside BFVs. As shown in Figure S5C, the product from physical mixture has negligible H_2O_2 scavenge ability, as demonstrated by nearly the same absorbance as control group. In sharp contrast, the $TiOSO_4$ absorbance in BFVs/CAT group was much lower. These results demonstrated the successful encapsulation of CAT in the BFVs by our co-extrusion procedure.

The TRAIL and PD-1 contents in BFVs were determined by ELISA (Figure S6), and the ratio to total proteins in BFVs was calculated to be 1.02% and 5.50%, respectively. To estimate the loading content of CAT, it was labeled with Cy5 prior to loading into BFVs; then, the CAT content was analyzed by fluorescence measurement (Figure S6), and the ratio to total proteins in BFVs was calculated to be 35.07%.

BFVs Block PDL1 on Cancer Cells to Increase Their Susceptibility to CTLs

The interaction between PD1 on activated CTLs ($CD8^+$ T cells) and its ligand PDL1 on cancer cells can exhaust CTLs and inhibit antitumor immune responses. Conversely, blockade of PD1/PDL1 axis could reverse this resistance and profoundly enhance therapeutic efficacy (Hirano et al., 2005). We next investigated whether our BFVs could act as a PDL1 checkpoint blockade. For this purpose, the 4T1 cells were incubated with FTIC-labeled PD1 presenting vesicles (BFVs/PD1) and imaged by CLSM. As shown in Figure 2A, BFVs/PD1 but not the control vesicles (without PD1 presenting, free NVs) could effectively bind to and be internalized by 4T1 cells after 4 h of incubation, but such binding and internalization could be blocked by PDL1 antibody pretreatment. To further intuitively demonstrate that the binding of BFVs/PD1 on 4T1 cells is mediated by the interaction between PD1 and PDL1, 4T1 cells were transfected with PDL1-EGFP plasmid to establish PDL1-EGFP expressing cells. Subsequently, the BFVs/PD1 with mCherry tag were incubated with these cells for 0.5 h at 4°C, then obvious co-localization with PDL1-EGFP on 4T1 cells was observed, in addition to some dissociative red fluorescence dots implying that BFVs/PD1 also might bind to endogenous PDL1 in 4T1 cells (Figure 2B). Similar results also could be observed in PDL1-EGFP-expressing H22 cells (Figure S7). Together, these results confirmed that the PD1-presenting BFVs could specifically interact with tumor cells through the binding between PD1 and PDL1.

We next attempted to explore whether the BFVs/PD1 could enhance the cytotoxicity of CTLs against cancer cells. As depicted in Figure 2C, naive mouse $CD8^+$ T cells were first isolated from the spleen of BALB/c

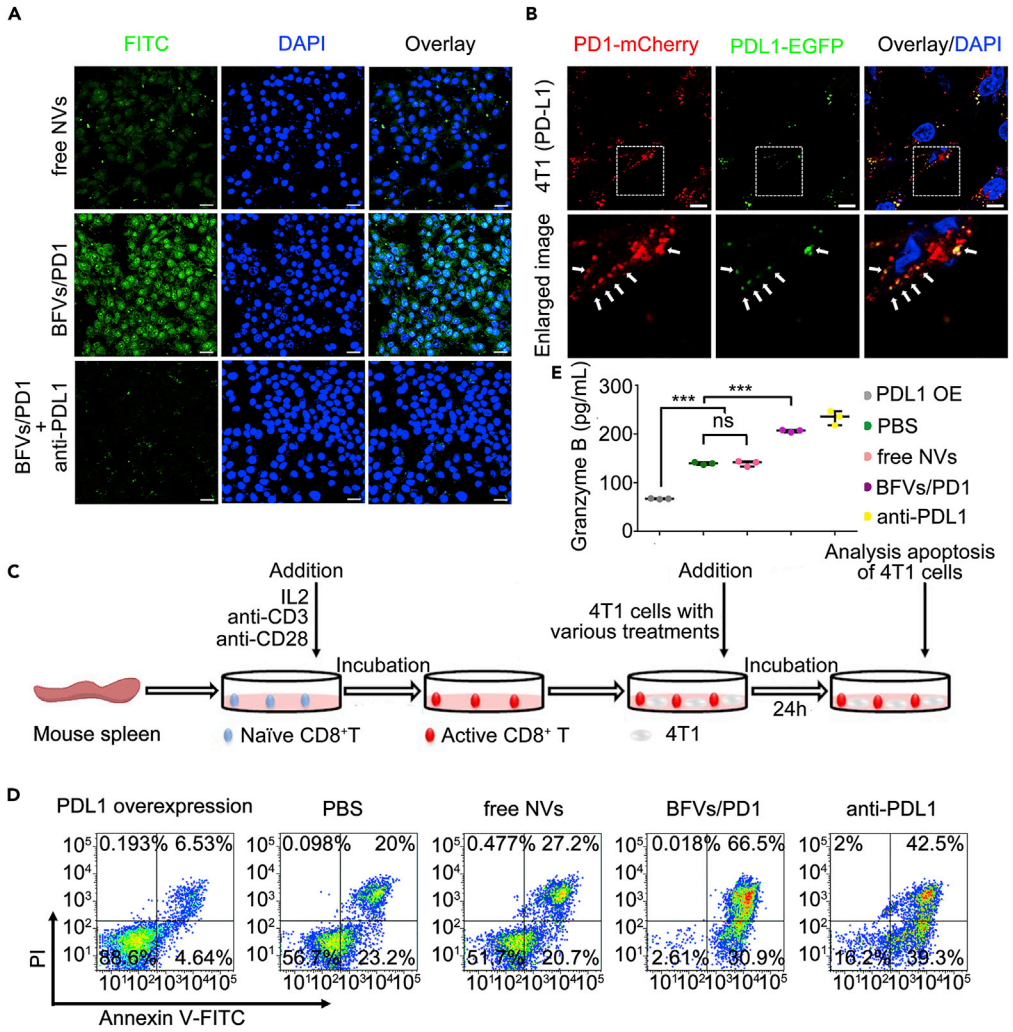

Figure 2. *In Vitro* Immune Checkpoint Inhibition of BFVs

(A) The CLSM images to present the internalization of FITC-labeled BFVs/PD1(50 μg/mL) by 4T1 breast cancer cells after 4 h of incubation (scale bar: 20 μm) at 37°C. free NVs: blank vesicles without presenting PD1 and TRAIL; BFVs/PD1: vesicles with surface presenting PD1 proteins; BFVs/PD1 + anti-PDL1: 4T1 cells pretreated with PDL1 antibody before BFVs/PD1 incubation.

(B) CLSM images to demonstrate the binding of BFVs/PD1-mCherry to the PDL1-EGFP over-expressed on 4T1 cell membrane (scale bar: 10 μm). 4T1 cells were transfected with PDL1-EGFP plasmid for 24 h, then incubated with BFVs/PD1-mCherry (50 μg/mL) for 0.5 h at 4°C. The lower panel is the enlarged image of the white dashed box on the upper panel.

(C) Representative procedure to schematically show the experimental design of the CTL cytotoxicity assay *in vitro*. Naive $CD8^+$ T cells extracted from mouse spleen were activated by incubation with IL2, anti-CD3, and anti-CD28 antibodies, then they were added into 4T1 cells that previously underwent various treatments indicated as below: 4T1 cells over-expressing PDL1 (PDL1 OE), or normal 4T1 cells treated with PBS (PBS), free NVs, BFVs/PD1, or PDL1 antibody (anti-PDL1). After 24 h of co-incubation, the apoptosis ratio of 4T1 cells was measured.

(D) Apoptosis of the 4T1 cells treated as mentioned above by using Annexin V-FITC and PI cell apoptosis assay.

(E) The Granzyme B secreted in the suspensions of co-culture system after 24 h of treatment. Data are expressed as min to max, show all points (ns, no significance; ***$p < 0.001$; $n = 3$).

mice by magnetic bead sorting, followed by CD3/CD28 antibody stimulation to obtain activated $CD8^+$ T cells. Subsequently, cancer cells with various treatments, such as blocking or overexpressing PDL1 on cell membranes, were added to the activated $CD8^+$ T cells to check the cytotoxic activity by using Annexin V-FITC and PI cell apoptosis (shortened as APCA) assay. The PDL1 overexpressing 4T1 cells were less susceptible to the activated $CD8^+$ T cells than the parental 4T1 cells; vice versa, when 4T1 cells were pretreated

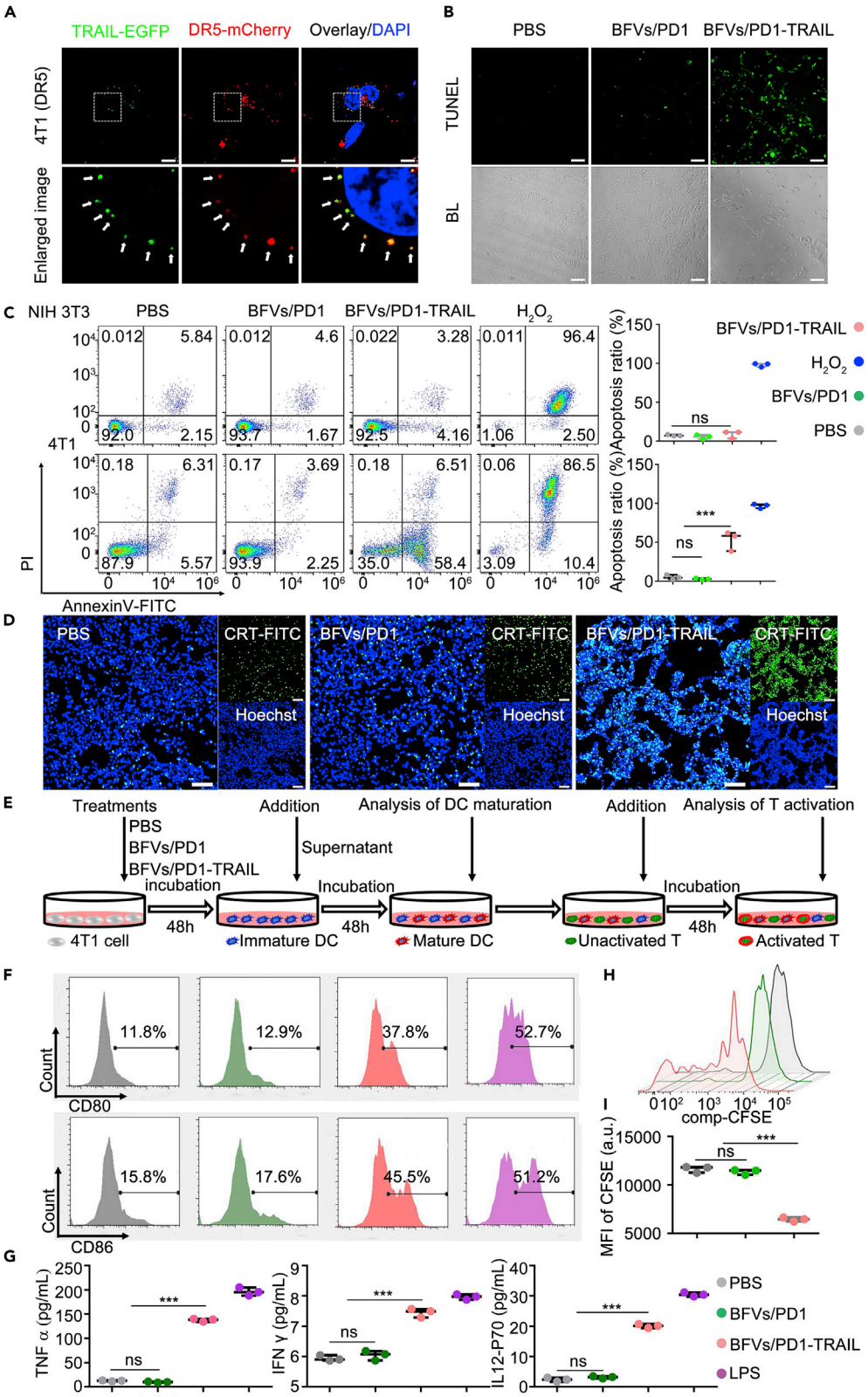
A
TRAIL-EGFP
DR5-mCherry
Overlay/DAPI
4T1 (DR5)
Enlarged image
B
PBS
BFVs/PD1
BFVs/PD1-TRAIL
TUNEL
BL
C
NIH 3T3
PBS
BFVs/PD1
BFVs/PD1-TRAIL
H2O2
4T1
PI
AnnexinV-FITC
Apoptosis ratio (%)
BFVs/PD1-TRAIL
H2O2
BFVs/PD1
PBS
ns
***
D
PBS
BFVs/PD1
BFVs/PD1-TRAIL
CRT-FITC
Hoechst
E
Treatments
PBS
BFVs/PD1
BFVs/PD1-TRAIL
incubation
48h
Addition
Supernatant
Analysis of DC maturation
Addition
Analysis of T activation
4T1 cell
Immature DC
Mature DC
Unactivated T
Activated T
F
Count
CD80
11.8%
12.9%
37.8%
52.7%
CD86
15.8%
17.6%
45.5%
51.2%
H
comp-CFSE
I
MFI of CFSE (a.u.)
ns
***
G
TNF α (pg/mL)
IFN γ (pg/mL)
IL12-P70 (pg/mL)
PBS
BFVs/PD1
BFVs/PD1-TRAIL
LPS

Figure 3. *In Vitro* ICD Responses of BFVs

(A) CLSM images to demonstrate the binding of BFVs/TRAIL-EGFP to the DR5-mCherry over-expressed on the 4T1 cells (scale bar: 10 μm). The 4T1 cells were transfected with DR5-mCherry plasmid for 24 h, then incubated with BFVs/TRAIL-EGFP (50 μg/mL) for 0.5 h at 4°C. The lower panel is the enlarged image of the white dashed box on the upper panel.

(B) TUNEL staining (green) and bright-field (BL) images of 4T1 cells with indicated treatments.

(C) Apoptosis of 4T1 cells with indicated treatments by flow cytometry analysis using Annexin V-FITC and PI staining, H_2O_2-treated cells were used as the positive control. The statistical analysis data are expressed as min to max, show all points (ns, no significance; ***$p < 0.001$; $n = 3$).

(D) The CLSM examination of CRT expression on the surface of 4T1 breast cancer cells (scale bar: 50 μm).

(E) Representative procedure to schematically show the experimental design of DC maturation and T cell activation assay *in vitro*. First, the tumor cells were treated as indicated to obtain supernatant. Then the supernatant was incubated with immature DCs for 48 h to trigger maturation. Finally, the matured DCs were co-cultured with $CD8^+$ T cells (pre-labeled with CFSE) for 72 h to trigger activation.

(F) The percentage of $CD80^+$ $CD86^+$ DCs through flow cytometry analysis after indicated treatments in the *in vitro* co-culture system, LPS-treated DC cells were used as the positive control.

(G) TNF-α, IFN-γ, and IL12-P70 levels in the supernatant of co-culture system after 2 days' treatment for DC maturation. Data are expressed as min to max, show all points (ns, no significance; ***$p < 0.001$; $n = 3$).

(H) The flow cytometry analysis of $CD8^+$ T cells labeled with CFSE 3 days after the co-culture.

(I) Mean fluorescence intensity (MFI) of CFSE labeled T cells. Data are expressed as min to max, show all points (ns, no significance; ***$p < 0.001$; $n = 3$).

by BFVs/PD1 or PDL1 antibody, they became significantly more susceptible (Figures 2D and S8). These results indicated that blocking of PDL1 on cancer cells by BFVs/PD1 could effectively reverse the inhibition of T cell-mediated cytotoxic activity harnessed by cancer cells. As a main route of carrying out immunosurveillance, CTLs can secrete granzymes to induce cancer cell death (Cullen et al., 2010). As shown in Figure 2E, it was clearly demonstrated that blocking PD1/PDL1 interactions by BFVs/PD1 could obviously induce tumor cell death through the release of Granzymes B from the activated $CD8^+$ T cells. These results strongly suggest that the BFVs/PD1 can block the PDL1 functions on cancer cells to re-strengthen T cell-mediated cytotoxic activity.

BFVs Induce ICD Responses in Cancer Cells

ICD plays an important role in initiating immune responses against tumor-associated antigens. Here, we further explore the potential of TRAIL as an ICD inducer, since it has been reported to selectively induce apoptosis by binding to the death receptors DR4 or DR5 in many cancer cell types while leaving normal cells unharmed (Jiang et al., 2016). Accordingly, we demonstrated that BFVs with surface presenting TRAIL-EGFP (BFVs/TRAIL) could co-localize with the DR5 on DR5-mCherry artificially over-expressed 4T1 cells or H22 cells (Figures 3A and S9). Meanwhile, TdT-mediated dUTP Nick-End Labeling (TUNEL) staining (Figure 3B) and APCA assay (Figures 3C and S10) demonstrated that the TRAIL on BFVs played a crucial role in inducing apoptosis of cancer cells (4T1 and H22) but not normal cells (NIH 3T3), whereas the PD1 proteins on BFVs had negligible effect. Calreticulin (CRT) is considered as one of the danger-associated molecular patterns (DAMPs) involved in ICD (Obeid et al., 2007). To confirm whether TRAIL on BFVs could promote ICD, the CRT expression of 4T1 cells with indicated treatments was analyzed by CLSM. As shown in Figure 3D, the CRT signals (green) dramatically increased in BFVs/PD1-TRAIL-treated group, compared with PBS or BFVs/PD1-treated groups.

The release of DAMPs together with tumor-associated antigens (TAAs) could promote the maturation of DCs and further enable the ability to prime T cell activation (Yue et al., 2019). To verify this, we carried out a series of experiments as illustrated in Figure 3E. The supernatant of 4T1 cells after above treatments were added into immature DCs collected from bone marrow cells after stimulating with granulocyte macrophage colony stimulating factor (GM-CSF). After 48 h of incubation, the DC maturation was evaluated by dual staining for CD80 and CD86, the typical markers on the surface of maturated DCs. It showed that the supernatant of cancer cells treated with BFVs/PD1-TRAIL could significantly improve the degree of DC maturation, as demonstrated by the higher percentage of CD80/CD86-positive DC cells (Figure 3F). Consistently, the levels of DC-secreted immune cytokines, such as TNF-α, IFN-γ, and IL12-P70 in supernatant also significantly increased after the BFVs/PD1-TRAIL treatment (Figure 3G). Afterward, the matured DCs were incubated with carboxyfluorescein succinimidyl ester (CSFE)-labeled $CD8^+$ T cells to explore their ability to prime T cell activation. The FACS analysis demonstrated that the matured DCs triggered by BFVs/PD1-TRAIL-treated cancer cells could significantly improve T cell proliferation (Figures 3H, 3I, and S11), compared with other groups without TRAIL component. Taken

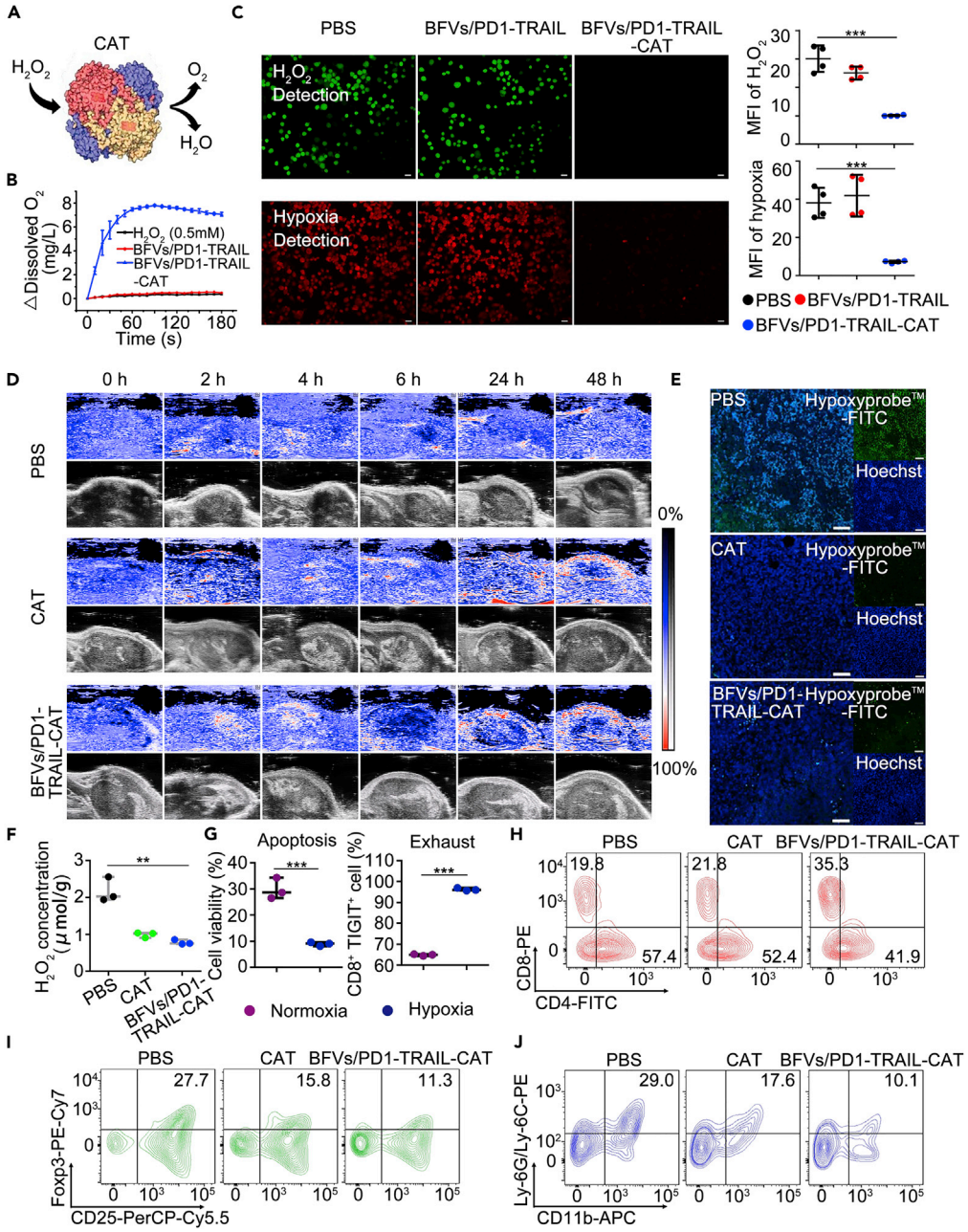

Figure 4. BFVs Alleviate Tumor Hypoxia to Enhance Intra-tumoral Infiltration of Effector T Cells and Relieve Immunosuppressive Tumor Microenvironment

(A) The schematic illustration of relieving tumor hypoxia through decomposing H_2O_2 into O_2 by CAT.

(B) Oxygen generation in H_2O_2 solutions (0.5 mM) with BFVs/PD1-TRAIL (without CAT) or BFVs/PD1-TRAIL-CAT (with CAT).

(C) Fluorescence microscopy images of 4T1 cells treated with BFVs/PD1-TRAIL and BFVs/PD1-TRAIL-CAT, whereas the cells treated with PBS were used as the control. The 4T1 cells were stained with Hydrogen Peroxide Assay Kit (green) or oxygen indicator of $[Ru(dpp)_3]Cl_2$ (red) (scale bar: 50 μm). The statistical analysis data are expressed as min to max, show all points (***$p < 0.001$; $n = 3$).

(D) Photoacoustic imaging to show the vascular saturated O_2 (sO_2) levels of tumor after *i.t.* injection of PBS, CAT, and BFVs/PD1-TRAIL-CAT at different time points. The black-white scale bar shows the ultrasound imaging signals and the blue-red scale bar shows the photoacoustic signals.

(E) Immunofluorescence staining of the tumor slices by using Hypoxyprobe-1 Plus Kits (green), scale bar: 50 μm.

Figure 4. *Continued*

(F) Intra-tumoral H_2O_2 concentration in the mice after 4 h of *i.t.* injection with PBS, CAT, and BFVs/PD1-TRAIL-CAT (**p < 0.01; n = 3).

(G) The flow cytometry analysis of the apoptosis and exhausting of $CD8^+$ T cells incubated under normoxic and hypoxic conditions by using APCA assay and TIGIT-PerCP-eFluor 710 staining (gated on $CD8^+$), respectively. The statistical analysis data are expressed as min to max, show all points (***p < 0.001; n = 3).

(H–J) The flow cytometry analysis of the frequency of effector T cells (h, gated on $CD3^+$), Tregs (I, gated on $CD4^+$), and MDSCs (J) inside the tumor treated with PBS, CAT, and BFVs/PD1-TRAIL-CAT for 2 days after *i.t.* injection.

together, these results suggest that the TRAIL rather than PD1 on BFVs is able to induce ICD responses in cancer cells to effectively mobilize host adaptive immunity, and it is an important aspect for changing the immune cold state of tumor.

BFVs Relieve Tumor Hypoxia to Enhance Intra-tumoral Infiltration of Effector T Cells and Deplete Immunosuppressive Cells

It has been reported that CAT could decompose H_2O_2 into O_2 (Figure 4A) (Chao et al., 2018); therefore, we wonder whether our BFVs with CAT in the inner core could *in situ* generate O_2 in the tumor microenvironment (with relatively high level of H_2O_2) to relieve tumor hypoxia. We first evaluated the ability of CAT in BFVs to generate O_2 in the presence of H_2O_2. As shown in Figure 4B, H_2O_2 and BFVs/PD1-TRAIL (without CAT loading) had negligible effect on O_2 generation, whereas the BFVs/PD1-TRAIL-CAT (with CAT loading) yielded significantly higher amounts of O_2 with H_2O_2 incubation. Afterward, we further explored the intracellular catalytic activity of BFVs/PD1-TRAIL-CAT by detecting H_2O_2 and O_2 levels in cells with different treatments under hypoxic condition. As expected, the cells treated with BFVs/PD1-TRAIL-CAT exhibited much weaker fluorescence of H_2O_2 and hypoxia indicators as compared with other control groups, suggesting the loaded CAT kept excellent enzyme activity to catalyze H_2O_2 into O_2 after internalization by cells (Figure 4C). For investigating the ability of relieving tumor hypoxia by BFVs/PD1-TRAIL-CAT *in vivo*, the oxygen saturation of tumors after local injection of BFVs/PD1-TRAIL-CAT was determined by photoacoustic imaging (PAI). Compared with the PBS group, the vascular saturated O_2 (sO_2) levels in the BFVs/PD1-TRAIL-CAT or free CAT-treated tumors were significantly higher (Figure 4D). To further confirm the relief of tumor hypoxia, the Hypoxyprobe-1 Plus Kits were used to assess the oxygenation status of tumor tissues. As shown in Figure 4E, the tumor treated with free CAT or BFVs/PD1-TRAIL-CAT showed dramatically decreased green fluorescence signal of hypoxia indicator. Concomitantly, the intra-tumoral H_2O_2 concentration in free CAT or BFVs/PD1-TRAIL-CAT-treated tumors was significantly lower than in the PBS-treated group (Figure 4F).

Emerging evidences demonstrated that tumor hypoxia could impair the antitumor immune responses by impeding killing function of CTLs, while promoting local immune suppression (Noman et al., 2015). Then, the influence of O_2 on the activation of $CD8^+$ T cells was first studied *in vitro*. After 48 h of culture, the primary $CD8^+$ T cells were admitted to APCA assay. The ratio of apoptotic $CD8^+$ T cells was significantly higher under hypoxic condition, compared with normoxic condition (Figures 4G, S12A, and S12B); the expression of TIGIT on $CD8^+$ T cells, a T cell exhausting marker (Joller et al., 2011), was also significantly up-regulated under hypoxic environment (Figures 4G, S12C, and S12D). Therefore, we anticipated the relief of hypoxia in TME might reverse the inhibition of antitumor immunity of $CD8^+$ effector T cells to some degree. To further explore the effects of relieving hypoxia on immune responses, we analyzed the infiltrated immune cell populations in tumors with different treatments after intra-tumoral (*i.t.*) injection by FACS analysis. The results showed that our BFVs/PD1-TRAIL-CAT not only could promote the intra-tumoral infiltration of $CD8^+$ T cells (Figures 4H and S13 and Tables S1 and S2) but also could deplete the immunosuppressive cells like Treg cells (Figures 4I and S14 and Table S3) and MDSCs (Figures 4J and S15 and Table S4). These results suggest that BFVs can remodel hypoxia TME and reverse the hypoxia-associated immunosuppression, which is crucial for converting immune cold tumor into hot.

In Vivo Antitumor Effect of BFVs

To evaluate the *in vivo* therapeutic effect of BFVs, a bilateral 4T1 tumor model was first established by subcutaneously (*s.c.*) injecting 1×10^6 and 5×10^5 4T1 tumor cells into the left and right flanks of mice as primary and abscopal tumors, respectively. The primary tumor received various treatments by *i.t.* injection at days 1, 4, 7, and 10 with the equivalent dosage (Figure 5A), while leaving the abscopal tumors untreated. Antitumor growth effects against the primary and abscopal tumors are summarized in Figures 5B and 5C.

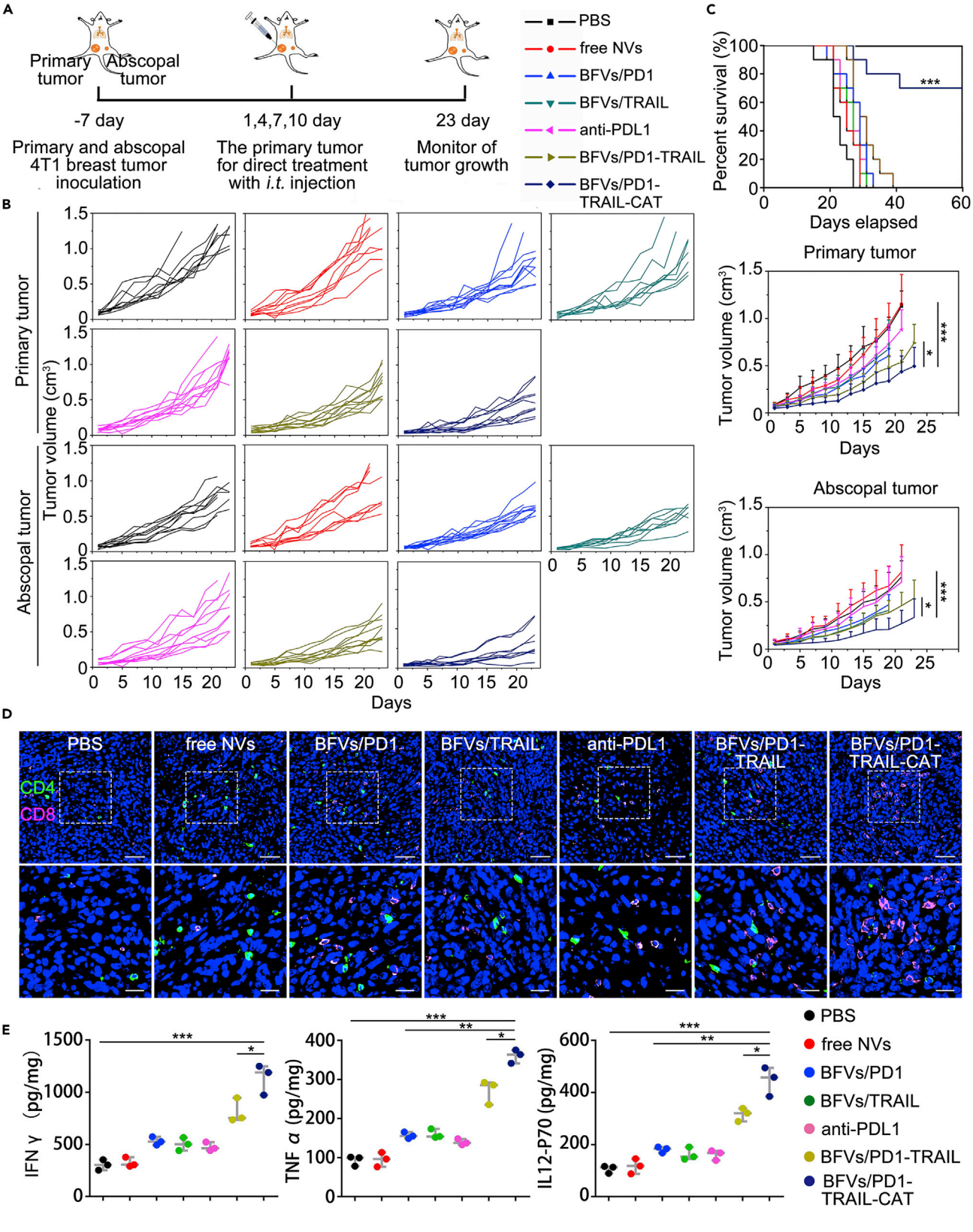
A
Primary tumor
Abscopal tumor
-7 day
Primary and abscopal 4T1 breast tumor inoculation
1,4,7,10 day
The primary tumor for direct treatment with i.t. injection
23 day
Monitor of tumor growth
PBS
free NVs
BFVs/PD1
BFVs/TRAIL
anti-PDL1
BFVs/PD1-TRAIL
BFVs/PD1-TRAIL-CAT
B
Primary tumor
Abscopal tumor
Tumor volume (cm³)
Days
C
Percent survival (%)
Days elapsed
***
Primary tumor
Tumor volume (cm³)
Days
Abscopal tumor
Tumor volume (cm³)
Days
D
PBS
free NVs
BFVs/PD1
BFVs/TRAIL
anti-PDL1
BFVs/PD1-TRAIL
BFVs/PD1-TRAIL-CAT
CD4
CD8
E
IFN γ (pg/mg)
TNF α (pg/mg)
IL12-P70 (pg/mg)
PBS
free NVs
BFVs/PD1
BFVs/TRAIL
anti-PDL1
BFVs/PD1-TRAIL
BFVs/PD1-TRAIL-CAT

Figure 5. Bilateral 4T1 Tumor Model Was Established to Evaluate the Abscopal Effect of BFVs

(A) Treatment schedule for BFVs-mediated immunotherapy. Tumors on the left were designated as the primary tumor for direct treatment with *i.t.* injection, and those on the right side were designated as distant tumor without treatment.

(B) Growth curves of the primary tumors and abscopal tumors after various treatments (PBS; free NVs; BFVs/PD1; BFVs/TRAIL; anti-PDL1, BFVs/PD1-TRAIL; BFVs/PD1-TRAIL-CAT). Average tumor volume of the treated mice in different groups (n = 8–10) (error bar, mean ± SD).

(C) Survival curves for the mice that received different treatments as indicated above (n = 10; ***p<0.001).

(D) Immunofluorescence staining of the tumor slices to show the infiltrated $CD4^+$ T cells (green) and $CD8^+$ T cells (pink) (scale bar: 100 μm). The lower panel is the enlarged image of the white dashed box on the upper panel (scale bar: 50 μm).

(E) The ELISA analysis of cytokine levels (IFN-γ, TNF-α, IL12-P70) in abscopal tumor from mice isolated at day 15 after *i.t.* injection for primary tumor. The statistical analysis data are expressed as min to max, show all points (*p < 0.05, **p < 0.01, ***p < 0.001; n = 3).

The primary tumors in the group of anti-PDL1, BFVs/PD1, BFVs/TRAIL, and BFVs/PD1-TRAIL treatment displayed slower tumor growth compared with the mice treated with PBS and blank vesicles without any functional components (free NVs). Notably, our BFVs containing PD1, TRAIL, and CAT (BFVs/PD1-TRAIL-CAT) exerted the highest antitumor efficacy among all groups, suggesting their synergistic effects. For abscopal tumors without direct treatment, the therapeutic outcomes are consistent with the primary tumors, with the highest therapeutic efficacy in BFVs/PD1-TRAIL-CAT-treated mice, and 70% of mice in this group survived for over 60 days, whereas all the mice in other groups survived no longer than 40 days, which might be attributed to the systematic activation of antitumor immunity. To verify this explanation, we analyzed the infiltration of TILs and the pro-inflammatory cytokines in abscopal tumors of the treated mice. As expected, BFVs/PD1-TRAIL-CAT-treated mice showed significantly promoted $CD8^+$ T cell infiltration (Figure 5D), as well as the highest level of TNF-α, IFN-γ, and IL12-P70 compared with other groups (Figure 5E), implying the cooperation of PD1, TRAIL, and CAT to deeply convert immune cold into hot, which in turn boosts the efficacy of immunotherapy.

Furthermore, we employed the orthotopic 4T1 tumor model, as it is more clinically relevant, to investigate the therapeutic effect of BFVs with systematic administration. The experimental protocol is shown in Figure 6A, wherein the orthotopic tumor model was established by injecting 5×10^5 4T1 cells into abdominal mammary fat pads of female BALB/c mice. Before therapeutic assessment, *in vivo* distribution of ICG-labeled vesicles was analyzed by NIR II fluorescence imaging system. It revealed that vesicles containing PD1 proteins (BFVs/PD1) had excellent tumor accumulation even after 48 h of injection, enabling their durable therapeutic effect (Figure S16). In addition, the tumor accumulation of BFVs/PD1 was significantly higher than the control vesicles (without PD1 presenting), ascribing to the targeting ability of PD1 to PDL1 on cancer cells rather than the difference of Pharmacokinetics (Figure S17). In contrast, free ICG, which was easily cleared out from the body, had negligible fluorescence signal in major organs including tumor tissue compared with BFVs (Figure S16). With regard to antitumor efficacy (Figures 6B–6D, S18, and S19), the overall trends of tumor growth inhibition on the orthotopic tumor model were approximately the same as those on the subcutaneously xenografted tumor model, highlighting the distinctive antitumor ability of BFVs/PD1-TRAIL-CAT owing to the synergistic contributions from TRAIL, PD1, and CAT to convert immune cold into hot. Histological examinations of the tumor tissues stained with H&E, TUNEL, and Ki67 also confirmed that our BFVs/PD1-TRAIL-CAT induced the most extensive level of tumor cell necrosis and apoptosis (Figures 6E and S20).

We next further explored the mechanisms underlying the remarkable antitumor efficiency of our BFVs-mediated synergistic therapy. First, immunofluorescent examination of tumor sections proved that the BFVs/PD1-TRAIL-CAT significantly increased CRT expression compared with other groups (Figure 6E). Since the CRT together with other DAMPs would promote the DC maturation for antigen presenting to T lymphocytes in draining lymph nodes (LNs), we analyzed the levels of DC maturation in draining LNs by FACS after 3 days of the last injection (Figure S21). As expected, the BFVs/PD1-TRAIL-CAT therapy triggered the highest level of DC maturation ($CD11c^+CD80^+CD86^+$) among all groups. Meanwhile, the intra-tumoral infiltration of T lymphocytes and immune-related cytokines were examined by multispectral immunofluorescence staining (Figure 6F) and ELISA (Figure 6G), respectively. It showed that the BFVs/PD1-TRAIL-CAT treatment triggered a significantly higher degree of $CD8^+$ T cell infiltration in tumors than other treatments. The cytokine secretion results also supported that BFVs/PD1-TRAIL-CAT treatment could elicit robust antitumor immune activity in tumor tissues, with the significantly increased secretion of pro-inflammation cytokines (TNF-α, IFN-γ, IL12-P70, Granzyme B) and decreased secretion of anti-inflammatory cytokines (TGF-β1, IL10). We also analyzed, in addition to tumor tissues, the frequency of T lymphocytes in peripheral blood by using FACS, and the result showed the percentage of $CD8^+$ T cells

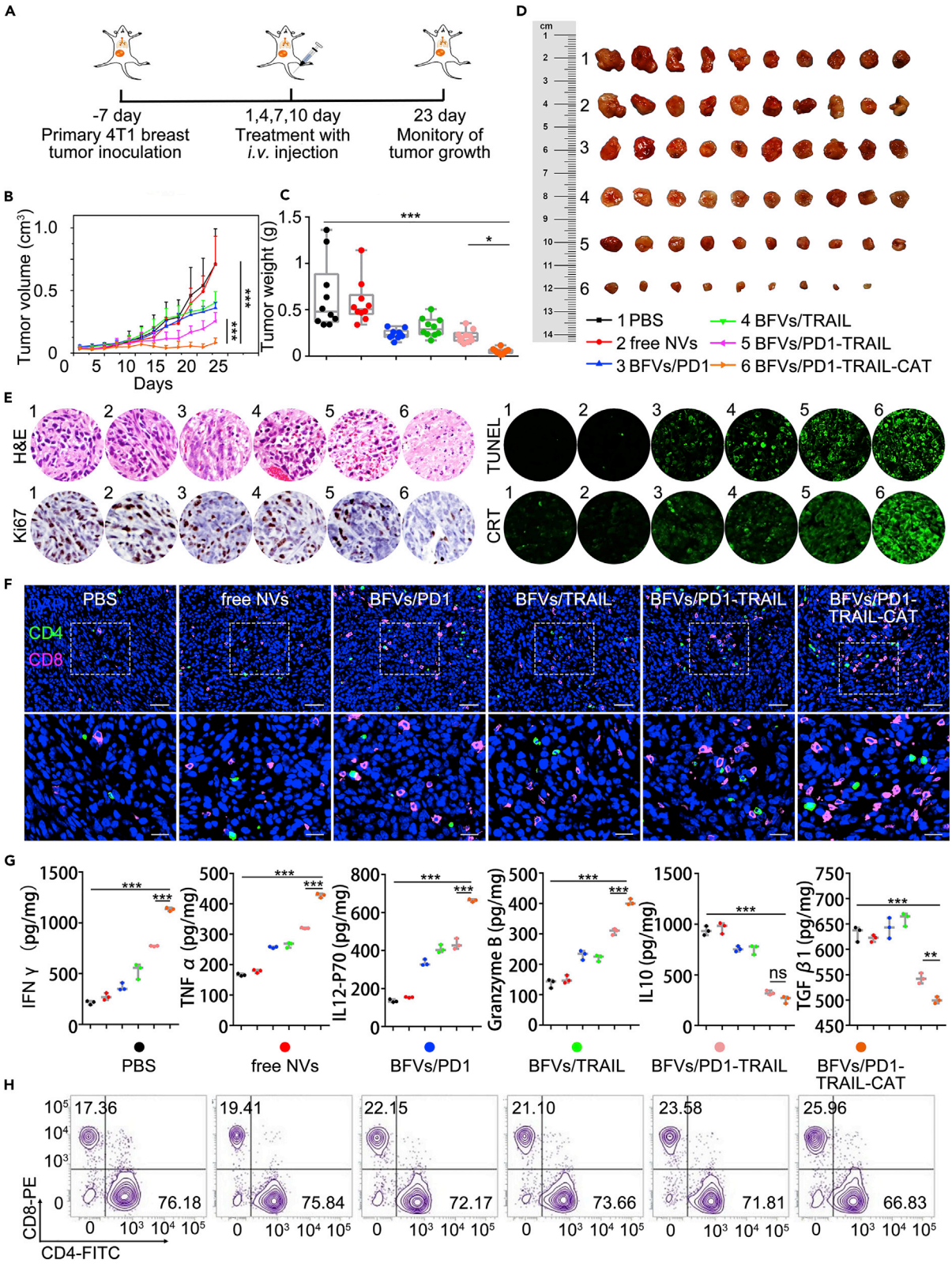
A
-7 day
Primary 4T1 breast tumor inoculation
1,4,7,10 day
Treatment with i.v. injection
23 day
Monitory of tumor growth
B
Tumor volume (cm3)
Days
C
Tumor weight (g)
D
cm
1 PBS
2 free NVs
3 BFVs/PD1
4 BFVs/TRAIL
5 BFVs/PD1-TRAIL
6 BFVs/PD1-TRAIL-CAT
E
H&E
Ki67
TUNEL
CRT
F
PBS
free NVs
BFVs/PD1
BFVs/TRAIL
BFVs/PD1-TRAIL
BFVs/PD1-TRAIL-CAT
DAPI
CD4
CD8
G
IFN γ (pg/mg)
TNF α (pg/mg)
IL12-P70 (pg/mg)
Granzyme B (pg/mg)
IL10 (pg/mg)
TGF β1 (pg/mg)
ns
H
CD8-PE
CD4-FITC
17.36
76.18
19.41
75.84
22.15
72.17
21.10
73.66
23.58
71.81
25.96
66.83

Figure 6. Orthotopic 4T1 Tumor Model Was Established to Evaluate the Antitumor Effect of BFVs

(A) Treatment schedule for the antitumor evaluation of BFVs on orthotopic 4T1 tumor model by *i.v.* injection.

(B) Average tumor volume of 4T1 tumors with indicated treatments. The statistical analysis data are expressed as min to max, show all points (***$p < 0.001$; n = 9–10).

(C) Average tumor weight of the mice that received indicated treatments at the day 23. The statistical analysis data are expressed as min to max, show all points (*$p < 0.05$, ***$p < 0.001$; n = 9–10).

(D) Photographs of tumor excised from sacrificed mice of each group at the day 23.

(E) Left panel: H&E and Ki67 antigen immunohistochemistry staining images of tumor slices in different groups. Right panel: TUNEL and anti-CRT immunofluorescence staining images of tumor slices in different group. 1: PBS; 2: free NVs; 3: BFVs/PD1; 4: BFVs/TRAIL; 5: BFVs/PD1-TRAIL; 6: BFVs/PD1-TRAIL-CAT.

(F) Immunofluorescence staining of the tumor slices to analyze the infiltrated $CD3^+$ T cells (red), $CD4^+$ T cells (green), and $CD8^+$ T cells (pink) (scale bar: 100 μm). The lower panel is the enlarged image of the white dashed box on the upper panel (scale bar: 50 μm).

(G) Cytokines levels in blood isolated from differently treated mice by ELISA analysis. The statistical analysis data are expressed as min to max, show all points (**$p < 0.01$, ***$p < 0.001$; n = 3).

(H) Representative plot analysis of T cells in blood isolated from differently treated mice by flow cytometry (gated on $CD3^+$).

in BFVs/PD1-TRAIL-CAT-treated groups was the highest compared with other groups, indicating the enhanced systemic immune responses after BFVs treatment (Figures 6H and S22). Taken together, these data suggest that the BFVs integrated functional components of TRAIL, PD1, and CAT could significantly boost systematic antitumor immune responses through converting immune cold into hot by simultaneously overcoming hypoxia, increasing immunogenic cell death, and checkpoint inhibition.

As the distinct characteristics of adaptive immune responses, immune-memory effects can provide long-term prevention against tumor recurrence and distant metastasis. Thus, we further assessed the immune-memory effects of our BFVs by *i.v.* infusion of 4T1 cells into the mice after the aforementioned treatments at day 30, whereas the residual tumor mass of each group was surgically resected from each mouse at the day 23. The animal experimental design is shown in Figure 7A. From photographs of the lung and H&E images (Figures 7B–7D), the PBS and free NVs-treated mice displayed large amounts of lung metastasis, whereas other control vesicle (BFVs/PD1, BFVs/TRAIL and BFVs/PD1-TRAIL)-treated mice showed certain degree of lung metastasis inhibition; as a remarkable contrast, the BFVs/PD1-TRAIL-CAT-treated mice showed almost no detectable metastasis, confirming the excellent immune memory effects after converting immune cold into hot.

To further identify the possible mechanisms of the long-term immune memory post synergistic immunotherapy of BFVs, we analyzed the central memory T cells (T_{CM}) and effector memory T cells (T_{EM}) in peripheral blood of mice after various treatments. Compared with T_{CM} only providing immunities in the condition of expansion, differentiation, and migration, T_{EM} can induce immediate protections upon secondary challenge (Ko and Formenti, 2018; McGranahan et al., 2016). As shown in Figures 7E–7I, S23, and S24, BFVs/PD1-TRAIL-CAT exhibited the highest frequency of $CD8^+$ T_{EM} and $CD4^+$ T_{EM} along with the lowest frequency of $CD8^+$ T_{CM} and $CD4^+$ T_{CM} in comparison with other groups, demonstrating the ability of our BFVs/PD1-TRAIL-CAT to shift systemic $CD8^+$ and $CD4^+$ T_{CM} cells toward a T_{EM} phenotype in the process of converting primary tumor from immune cold into hot, which is responsible for generating more-potent antitumor immune memory responses to prevent recurrence.

DISCUSSION

With a review of the recent developments of tumor immunotherapy, the combination paradigms of conventional therapeutic modalities with ICB have shown great potency to augment cancer immunotherapy efficacy, but their effectiveness largely depends on the baseline immune responses. In such a case, most of solid tumors featured as immune cold lacking pre-existing adaptive immunity do not respond well to the current combinational therapeutic strategies (Galon and Bruni, 2019). Another concern with the present approaches would be the concurrent increase in undesired side effects (Whiteside et al., 2016). The main mechanisms involved in cold tumor include lack of TAA burden, deficient and exhausted TILs, and hypoxic TME-driven immunosuppressive environment. Conventional therapeutic modalities (e.g., radiotherapy, chemotherapy) can augment the antigenicity of tumor cells through increasing the release of TAAs, whereas these released TAAs are often poorly processed, presented, and recognized by immune cells owing to the extensive existing immune-suppression mechanisms; thus, the immune responses in such case are generally very limited (McGranahan et al., 2016). Meanwhile, like a double-edged sword, radiotherapy or chemotherapy can also subvert tumor immunosurveillance through recruiting myeloid cell types

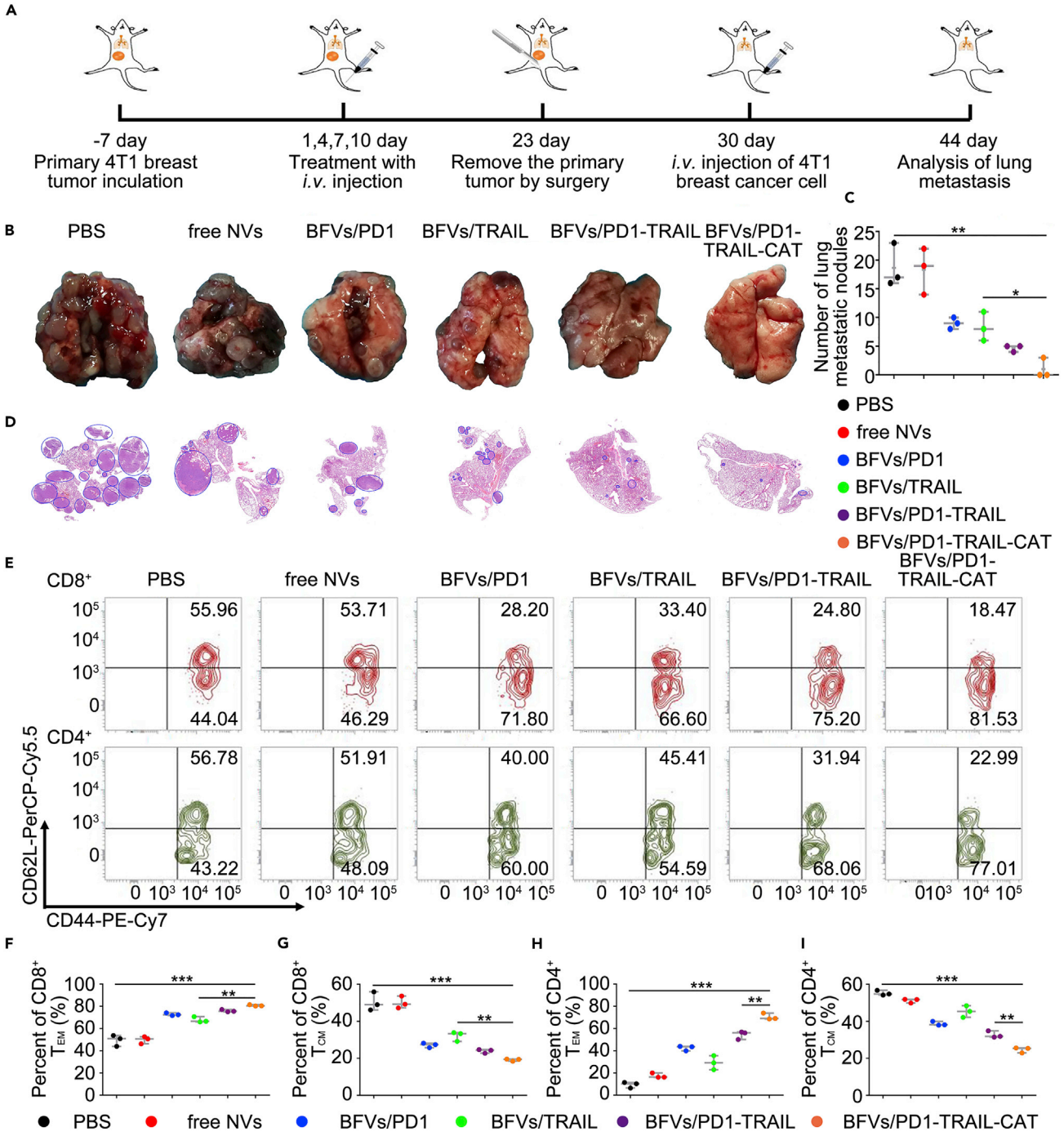

Figure 7. Long-Term Immune-Memory Effect of BFVs

(A) Schematic illustration of BFV treatment for lung metastasis inhibition of 4T1 tumor in BALB/c mice.

(B) Photographs of the lungs excised from sacrificed mice of each group.

(C) Statistical analysis of lung metastasis nodules (*$p < 0.05$, **$p < 0.01$; $n = 3$).

(D) H&E staining images of lung metastasis slices in different groups.

(E) Flow cytometry analysis of the T_{CM} and T_{EM} in peripheral blood isolated from sacrificed mice after various treatments by staining CD44-PE-Cy7 and CD62L-PerCP-Cy5.5.

(F–I) The statistical analysis for the percentage of the T_{CM} and T_{EM} in CD8+ or CD4+ T cells, data are expressed as min to max, show all points (**$p < 0.01$, ***$p < 0.001$; $n = 3$).

with distinct roles in T cell suppression and other side effects on normal tissue (Ko and Formenti, 2018). To restore the exhausted TILs, monoclonal antibody such as checkpoint inhibitor has gained considerable success in a subset of patients, but it also suffers from inefficient delivery into targeted site and severe immune-related adverse events (Naidoo et al., 2015). With respect to remodeling TME, respiratory hyperoxia (60% oxygen) has been verified to decrease intra-tumoral hypoxia for promoting antitumor immune response, whereas this systemic O_2 supply approach might cause acute lung injury (Kallet and Matthay, 2013). Thus, how to simultaneously, safely, and effectively overcome these obstacles (converting tumor from immune cold into hot) is the key challenge for boosting robust immune responses to fight against cold tumors.

Compared with the existing therapeutic approaches that failed to turn cold tumor into hot milieu, our BFVs integrating PD1, TRAIL, and CAT showed several distinct merits and could efficiently convert cold tumor into hot. In our design, the TRAIL could selectively elicit ICD of cancer cells, whereas it had limited toxicity on normal cells; the CAT in BFVs not only could *in situ* generate O_2 by virtue of the high levels of H_2O_2 in cancer cells without producing pulmonary O_2 toxicity but also could reduce the malignant biological roles caused by H_2O_2 including metastasis of cancer cells, angiogenesis, and resistance to therapies (López-Lázaro, 2007). Furthermore, all components in our BFVs belong to biomolecules whose biological functions are nicely preserved in TME and have excellent biocompatibility and biodegradability without any noticeable toxicities (Figures S25–S29). Therefore, our BFVs integrating PD1, TRAIL, and CAT could effectively convert immune cold into hot through simultaneously overcoming hypoxia, inducing ICD and immune checkpoint inhibition. As a result, our BFVs not only boosted robust and systemic antitumor immune responses that simultaneously inhibited primary and abscopal tumor growth but also achieved long-term immune memory effects to prevent tumor recurrence/metastasis. In principle, our reported BFVs also could be suitable for the immunotherapy of other solid tumors. Thus, our approach might be particularly meaningful and readily adapted to a broad diversity of immune cold tumors that do not respond well to ICB therapies.

Limitations of the Study

The BFVs proposed here have comprehensive immuno-modulating ability to elicit robust and systematic antitumor immunity, but their antitumor efficiency might be heavily affected by the heterogeneity of cancer cells, tumor microenvironment, and patients' baseline immunity, which are very difficult to precisely measure and predict. Furthermore, the exact components of naturally obtained cell membranes are very difficult to accurately determine and quantify, which might be an obstacle for pharmaceutical translation, owing to difficulty in getting the same quality BFVs from batch to batch, and also lack of precise quality control strategy for large-scale production. These limitations should be further resolved for future translational applications.

Resource Availability

Lead Contact

Further information and requests for resources should be directed to and will be fulfilled by the Lead Contact, Xiaolong Liu (xiaoloong.liu@gmail.com).

Materials Availability

This study did not generate new unique materials.

Data and Code Availability

All data produced or analyzed for this study are included in the published article and its supplementary information files.

METHODS

All methods can be found in the accompanying Transparent Methods supplemental file.

SUPPLEMENTAL INFORMATION

Supplemental Information can be found online at https://doi.org/10.1016/j.isci.2020.101341.

ACKNOWLEDGMENTS

This work was supported by the National Natural Science Foundation of China (Grant No. 61727823, 81671813, 81601538), the joint research projects of Health and Education Commission of Fujian Province (Grant No. 2019-WJ-20).

AUTHOR CONTRIBUTIONS

M.W., D.Zheng., and D.Zhang. contributed equally to this work; M.W., J.Liu., and X.Liu. designed the project; M.W., D.Zheng., D.Zhang., P.Y., L.P., F.C., Z.L., Z.C., J.Li., Z.W., and X.Lin. conducted the experiments; M.W., D.Zheng., and D.Zhang. analyzed and interpreted the data; X.Liu. and J.Liu. supervised the overall research; M.W., D.Zheng., and X.Liu. wrote the manuscript.

DECLARATION OF INTERESTS

The authors declare no competing interests.

Received: March 2, 2020
Revised: June 1, 2020
Accepted: July 2, 2020
Published: July 24, 2020

REFERENCES

Binnewies, M., Roberts, E.W., Kersten, K., Chan, V., Fearon, D.F., Merad, M., Coussens, L.M., Gabrilovich, D.I., Ostrand-Rosenberg, S., and Hedrick, C.C. (2018). Understanding the tumor immune microenvironment (TIME) for effective therapy. Nat. Med. *24*, 541–550.

Boussiotis, V.A. (2016). Molecular and biochemical aspects of the PD-1 checkpoint pathway. N. Engl. J. Med. *375*, 1767–1778.

Chao, Y., Xu, L., Liang, C., Feng, L., Xu, J., Dong, Z., Tian, L., Yi, X., Yang, K., and Liu, Z. (2018). Combined local immunostimulatory radioisotope therapy and systemic immune checkpoint blockade imparts potent antitumour responses. Nat. Biomed. Eng. *2*, 611.

Chen, Q., Chen, G., Chen, J., Shen, J., Zhang, X., Wang, J., Chan, A., and Gu, Z. (2019). Bioresponsive protein complex of aPD1 and aCD47 antibodies for enhanced immunotherapy. Nano Lett. *19*, 4879–4889.

Chiang, C.-S., Lin, Y.-J., Lee, R., Lai, Y.-H., Cheng, H.-W., Hsieh, C.-H., Shyu, W.-C., and Chen, S.-Y. (2018). Combination of fucoidan-based magnetic nanoparticles and immunomodulators enhances tumour-localized immunotherapy. Nat. Nanotechnol *13*, 746–754.

Cullen, S., Brunet, M., and Martin, S. (2010). Granzymes in cancer and immunity. Cell Death Differ *17*, 616–623.

Galon, J., and Bruni, D. (2019). Approaches to treat immune hot, altered and cold tumours with combination immunotherapies. Nat. Rev. Drug Discov. *18*, 197–218.

Galstyan, A., Markman, J.L., Shatalova, E.S., Chiechi, A., Korman, A.J., Patil, R., Klymyshyn, D., Tourtellotte, W.G., Israel, L.L., Braubach, O., et al. (2019). Blood–brain barrier permeable nano immunoconjugates induce local immune responses for glioma therapy. Nat. Commun. *10*, 3850.

Hatfield, S.M., Kjaergaard, J., Lukashev, D., Schreiber, T.H., Belikoff, B., Abbott, R., Sethumadhavan, S., Philbrook, P., Ko, K., and Cannici, R. (2015). Immunological mechanisms of the antitumor effects of supplemental oxygenation. Hatfield *7*, 277ra230.

He, C., Duan, X., Guo, N., Chan, C., Poon, C., Weichselbaum, R.R., and Lin, W. (2016). Core-shell nanoscale coordination polymers combine chemotherapy and photodynamic therapy to potentiate checkpoint blockade cancer immunotherapy. Nat. Commun. *7*, 12499.

Hirano, F., Kaneko, K., Tamura, H., Dong, H., Wang, S., Ichikawa, M., Rietz, C., Flies, D.B., Lau, J.S., Zhu, G., et al. (2005). Blockade of B7-H1 and PD-1 by monoclonal antibodies potentiates cancer therapeutic immunity. Cancer Res. *65*, 1089–1096.

Huang, L., Li, Y., Du, Y., Zhang, Y., Wang, X., Ding, Y., Yang, X., Meng, F., Tu, J., Luo, L., et al. (2019). Mild photothermal therapy potentiates anti-PD-L1 treatment for immunologically cold tumors via an all-in-one and all-in-control strategy. Nat. Commun. *10*, 4871.

Jiang, X., Fitch, S., Wang, C., Wilson, C., Li, J., Grant, G.A., and Yang, F. (2016). Nanoparticle engineered TRAIL-overexpressing adipose-derived stem cells target and eradicate glioblastoma via intracranial delivery. PNAS *113*, 13857–13862.

Joller, N., Hafler, J.P., Brynedal, B., Kassam, N., Spoerl, S., Levin, S.D., Sharpe, A.H., and Kuchroo, V.K. (2011). Cutting edge: TIGIT has T cell-intrinsic inhibitory functions. J. Immunol. *186*, 1338–1342.

Kallet, R.H., and Matthay, M.A. (2013). Hyperoxic acute lung injury. Respir. Care *58*, 123–141.

Kim, T.K., Herbst, R.S., and Chen, L. (2018). Defining and understanding adaptive resistance in cancer immunotherapy. Trends Immunol. *39*, 624–631.

Ko, E.C., and Formenti, S.C. (2018). Radiotherapy and checkpoint inhibitors: a winning new combination? Ther. Adv. Med. Oncol. *10*, https://doi.org/10.1177/1758835918768240.

Liu, X., Liu, C., Zheng, Z., Chen, S., Pang, X., Xiang, X., Tang, J., Ren, E., Chen, Y., You, M., et al. (2019). Vesicular antibodies: a bioactive multifunctional combination platform for targeted therapeutic delivery and cancer immunotherapy. Adv. Mater. *31*, 1808294.

López-Lázaro, M. (2007). Dual role of hydrogen peroxide in cancer: possible relevance to cancer chemoprevention and therapy. Cancer Lett. *252*, 1–8.

McGranahan, N., Furness, A.J., Rosenthal, R., Ramskov, S., Lyngaa, R., Saini, S.K., Jamal-Hanjani, M., Wilson, G.A., Birkbak, N.J., and Hiley, C.T. (2016). Clonal neoantigens elicit T cell immunoreactivity and sensitivity to immune checkpoint blockade. Science *351*, 1463–1469.

Mi, Y., Smith, C.C., Yang, F., Qi, Y., Roche, K.C., Serody, J.S., Vincent, B.G., and Wang, A.Z. (2018). A dual immunotherapy nanoparticle improves T-cell activation and cancer immunotherapy. Adv. Mater. *30*, 1706098.

Naidoo, J., Page, D., Li, B., Connell, L., Schindler, K., Lacouture, M., Postow, M., and Wolchok, J. (2015). Toxicities of the anti-PD-1 and anti-PD-L1 immune checkpoint antibodies. Ann. Oncol. *26*, 2375–2391.

Noman, M.Z., Hasmim, M., Messai, Y., Terry, S., Kieda, C., Janji, B., and Chouaib, S. (2015). Hypoxia: a key player in antitumor immune response. A review in the theme: cellular responses to hypoxia. Am. J. Physiol-cell Ph *309*, C569–C579.

Obeid, M., Tesniere, A., Ghiringhelli, F., Fimia, G.M., Apetoh, L., Perfettini, J.-L., Castedo, M., Mignot, G., Panaretakis, T., and Casares, N. (2007). Calreticulin exposure dictates the

immunogenicity of cancer cell death. Nat. Med. *13*, 54–61.

Robert, C., Schachter, J., Long, G.V., Arance, A., Grob, J.J., Mortier, L., Daud, A., Carlino, M.S., McNeil, C., and Lotem, M. (2015). Pembrolizumab versus ipilimumab in advanced melanoma. N. Engl. J. Med. *372*, 2521–2532.

Ruan, H., Hu, Q., Wen, D., Chen, Q., Chen, G., Lu, Y., Wang, J., Cheng, H., Lu, W., and Gu, Z. (2019). A dual-bioresponsive drug-delivery depot for combination of epigenetic modulation and immune checkpoint blockade. Adv. Mater. *31*, 1806957.

Sagiv-Barfi, I., Kohrt, H.E.K., Czerwinski, D.K., Ng, P.P., Chang, B.Y., and Levy, R. (2015). Therapeutic antitumor immunity by checkpoint blockade is enhanced by ibrutinib, an inhibitor of both BTK and ITK. PNAS *112*, E966–E972.

Tang, J., Yu, J.X., Hubbard-Lucey, V.M., Neftelinov, S.T., Hodge, J.P., and Lin, Y. (2018). The clinical trial landscape for PD1/PDL1 immune checkpoint inhibitors. Nat. Rev. Drug Discov. *17*, 854–855.

Topalian, S.L., Hodi, F.S., Brahmer, J.R., Gettinger, S.N., Smith, D.C., McDermott, D.F., Powderly, J.D., Carvajal, R.D., Sosman, J.A., and Atkins, M.B. (2012). Safety, activity, and immune correlates of anti–PD-1 antibody in cancer. N. Engl. J. Med. *366*, 2443–2454.

Tumeh, P.C., Harview, C.L., Yearley, J.H., Shintaku, I.P., Taylor, E.J., Robert, L., Chmielowski, B., Spasic, M., Henry, G., and Ciobanu, V. (2014). PD-1 blockade induces responses by inhibiting adaptive immune resistance. Nature *515*, 568.

von Karstedt, S., Montinaro, A., and Walczak, H. (2017). Exploring the TRAILs less travelled: TRAIL in cancer biology and therapy. Nat. Rev. Cancer *17*, 352.

Wang, C., Sun, W., Wright, G., Wang, A.Z., and Gu, Z. (2016). Inflammation-triggered cancer immunotherapy by programmed delivery of CpG and anti-PD1 antibody. Adv. Mater. *28*, 8912–8920.

Wang, C., Wang, J., Zhang, X., Yu, S., Wen, D., Hu, Q., Ye, Y., Bomba, H., Hu, X., and Liu, Z. (2018). In situ formed reactive oxygen species–responsive scaffold with gemcitabine and checkpoint inhibitor for combination therapy. Sci. Transl. Med. *10*, eaan3682.

Wang, D., Wang, T., Yu, H., Feng, B., Zhou, L., Zhou, F., Hou, B., Zhang, H., Luo, M., and Li, Y. (2019). Engineering nanoparticles to locally activate T cells in the tumor microenvironment. Sci. Immunol. *4*, eaau6584.

Whiteside, T.L., Demaria, S., Rodriguez-Ruiz, M.E., Zarour, H.M., and Melero, I. (2016). Emerging opportunities and challenges in cancer immunotherapy. Clin. Cancer Res. *22*, 1845–1855.

Wolchok, J.D., Kluger, H., Callahan, M.K., Postow, M.A., Rizvi, N.A., Lesokhin, A.M., Segal, N.H., Ariyan, C.E., Gordon, R.-A., and Reed, K. (2013). Nivolumab plus ipilimumab in advanced melanoma. N. Engl. J. Med. *369*, 122–133.

Yue, W., Chen, L., Yu, L., Zhou, B., Yin, H., Ren, W., Liu, C., Guo, L., Zhang, Y., and Sun, L. (2019). Checkpoint blockade and nanosonosensitizer-augmented noninvasive sonodynamic therapy combination reduces tumour growth and metastases in mice. Nat. Commun. *10*, 2025.

Zhang, P., Zhang, L., Qin, Z., Hua, S., Guo, Z., Chu, C., Lin, H., Zhang, Y., Li, W., Zhang, X., et al. (2018a). Genetically engineered liposome-like nanovesicles as active targeted transport platform. Adv. Mater. *30*, 1705350.

Zhang, X., Wang, C., Wang, J., Hu, Q., Langworthy, B., Ye, Y., Sun, W., Lin, J., Wang, T., and Fine, J. (2018b). PD-1 blockade cellular vesicles for cancer immunotherapy. Adv. Mater. *30*, 1707112.

Zhang, X., Wang, J., Chen, Z., Hu, Q., Wang, C., Yan, J., Dotti, G., Huang, P., and Gu, Z. (2018c). Engineering PD-1-presenting platelets for cancer immunotherapy. Nano Lett. *18*, 5716–5725.

Zou, W., Wolchok, J.D., and Chen, L. (2016). PD-L1 (B7-H1) and PD-1 pathway blockade for cancer therapy: mechanisms, response biomarkers, and combinations. Sci. Transl. Med. *8*, 328rv324.

iScience, Volume *23*

Supplemental Information

Converting Immune Cold into Hot by Biosynthetic Functional Vesicles to Boost Systematic Antitumor Immunity

Ming Wu, Dongye Zheng, Da Zhang, Peiwen Yu, Lianli Peng, Feng Chen, Ziguo Lin, Zhixiong Cai, Jiong Li, Zuwu Wei, Xinyi Lin, Jingfeng Liu, and Xiaolong Liu

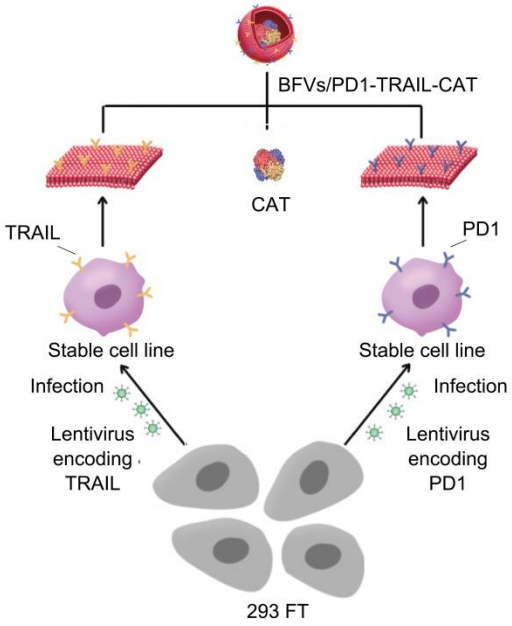

Figure S1. Schematic illustration of the preparation of BFVs/PD1-TRAIL-CAT. Related to Figure 1.

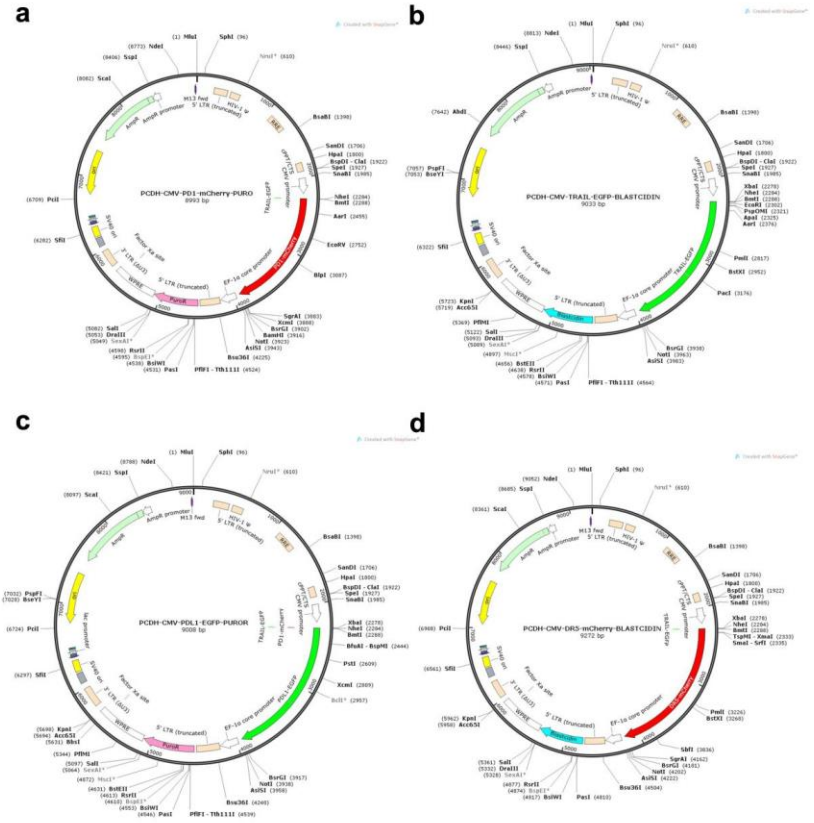

Figure S2. The information of plasmids used in this study. (a) PCDH-CMV-PD1-mCherry-PURO. (b) PCDH-CMV-TRAIL-EGFP-BLASTCIDIN. (c) PCDH-CMV-PDL1-EGFP-PURO. (d) PCDH-CMV-DR5-mCherry-BLASTCIDIN. Related to Figure 1.

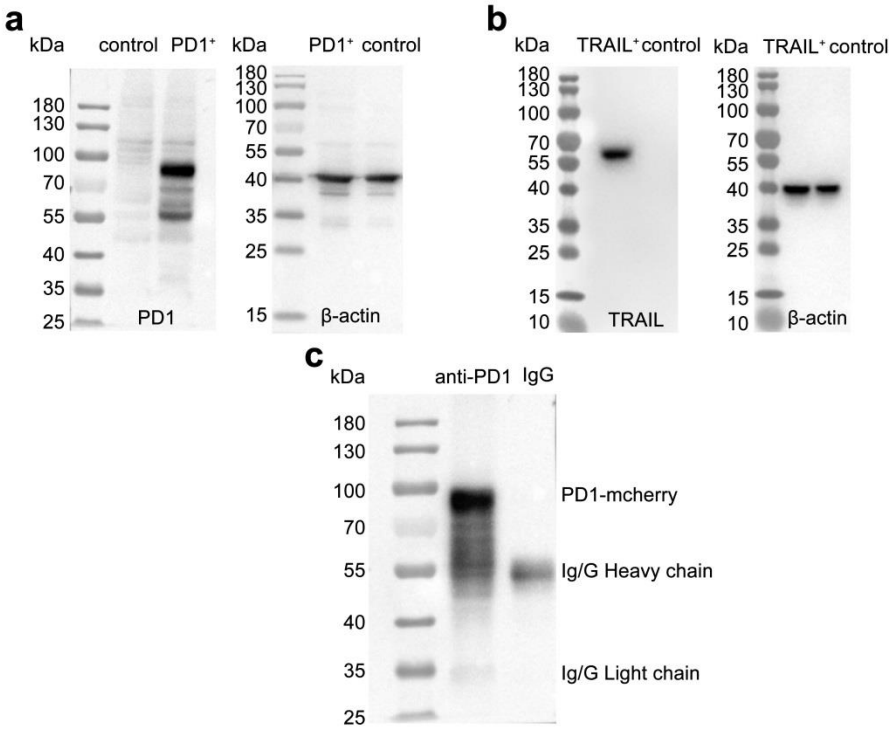

Figure S3. Full gel scan images. (a, b) Uncropped blot of Figure 1d. (c) Uncropped blot of Figure 1h. Related to Figure 1.

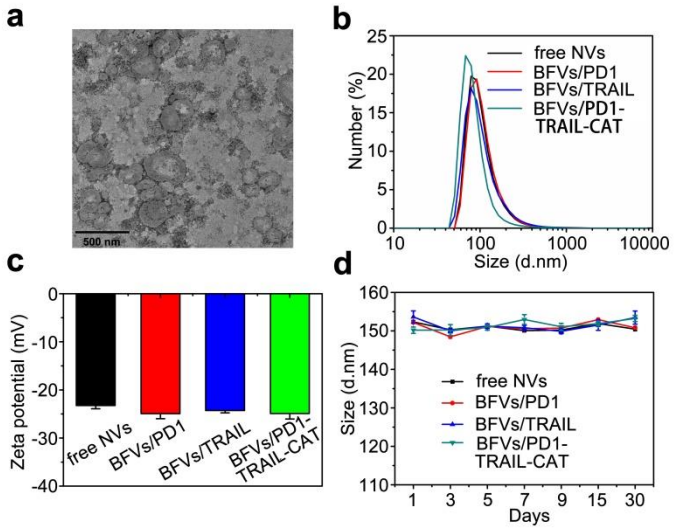

Figure S4. (a) The transmission electron microscopy image of BFVs (scale bar: 50 nm). (b) The size distribution of free NVs, BFVs/PD1, BFVs/TRAIL and BFVs/PD1-TRAIL-CAT measured by DLS. (c) The zeta potential of free NVs, BFVs/PD1, BFVs/TRAIL and BFVs/PD1-TRAIL-CAT (n=3). Error bar, mean±s.d. c. The stability of free NVs, BFVs/PD1, BFVs/TRAIL and BFVs/PD1-TRAIL-CAT measured by DLS (n=3). Error bar, mean±s.d. (d) The stability of free NVs, BFVs/PD1, BFVs/TRAIL and BFVs/PD1-TRAIL-CAT which were stored in MEM (without Phenol Red) supplemented with 10% FBS up to 30 days, were measured by DLS (n=3). Error bar, mean±s.d. free NVs: blank vesicles without any functional components; BFVs/PD1: vesicles with surface presenting PD1 proteins; BFVs/TRAIL: vesicles with surface presenting TRAIL proteins; BFVs/PD1-TRAIL-CAT: final vesicles with surface presenting PD1 and TRAIL proteins, and inner core encapsulating CAT. Related to Figure 1.

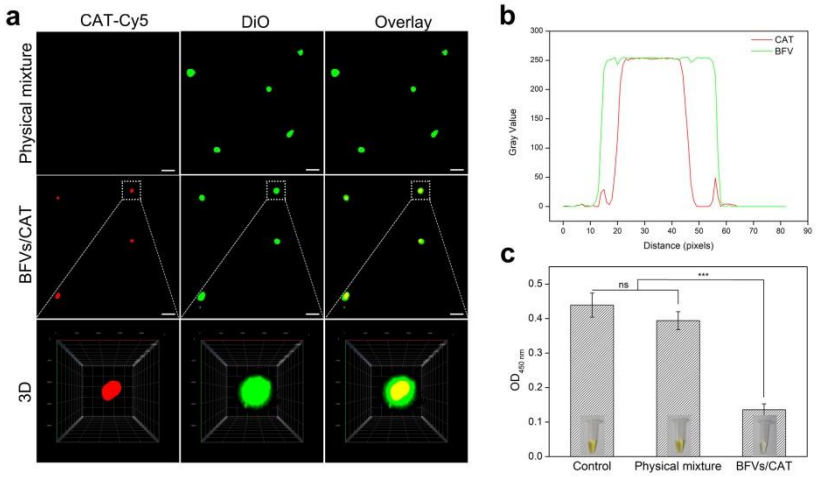

Figure S5. (a) Confocal images to demonstrate the encapsulation of CAT in BFVs. 3D reconstruction of Z-stack images is resulted from the representative fluorescent vesicle marked by the dashed rectangular frame. Scale bar: 20 μm. (b) Plot profiles along the single merged fluorescence vesicle. (c) $TiOSO_4$ as a probe to monitor the enzyme activity after H_2O_2 addition to the final products from BFVs and CAT physical mixture or from the co-extrusion procedure. Related to Figure 1.

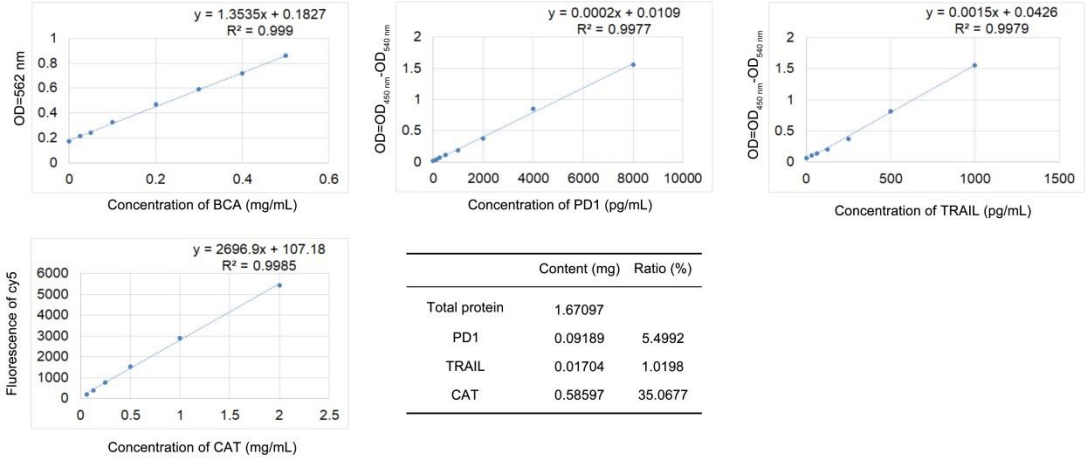

	Content (mg)	Ratio (%)
Total protein	1.67097	
PD1	0.09189	5.4992
TRAIL	0.01704	1.0198
CAT	0.58597	35.0677

Figure S6. The specific ratio and content of TRAIL, PD-1 and CAT in BFVs, where the total protein was determined by BCA assay, and the PD1 and TRAIL were determined by ELISA, CAT was determined by fluorescence measurement. Related to Figure 1.

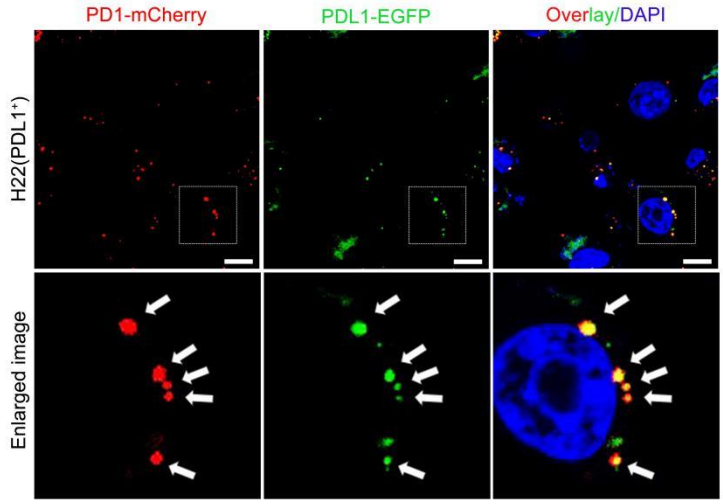

Figure S7. The CLSM images to show the co-localization of BFVs/PD1-mCherry with the overexpressed PDL1-EGFP on H22 cells. The H22 cells were transfected with PDL1-EGFP plasmid for 24 h, then incubated with BFVs/PD1-mCherry (50 μg/mL) for 0.5 h at 4 ℃. The lower panel is the enlarged images of the white dashed box on the upper panel. Scale bar: 10μm. Related to Figure 2.

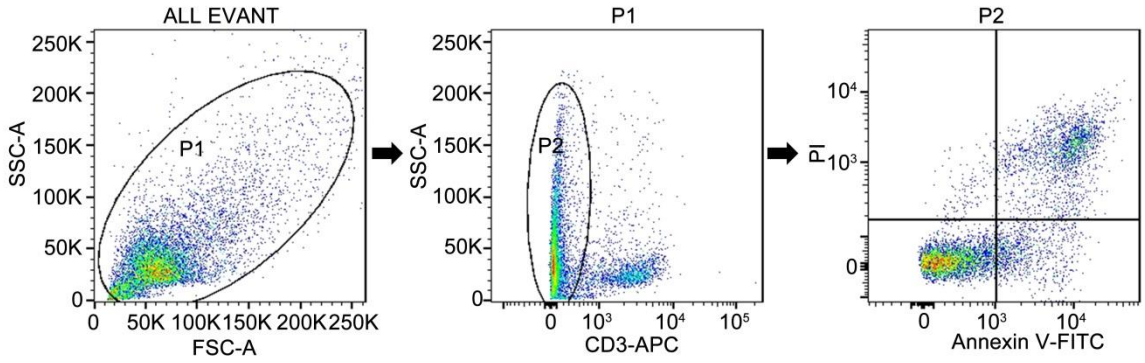

Figure S8. Representative FACS gating strategy for detecting the cytotoxicity of CTLs in the co-incubation system with CTLs and 4T1 breast cancer cells. Related to Figure 2.

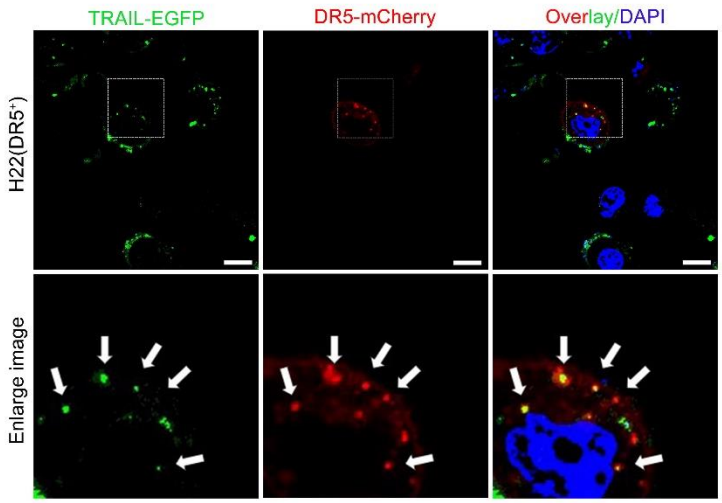

Figure S9. CLSM images to show the co-localization of BFVs/TRAIL-EGFP with the over-expressed DR5-mCherry on H22 cells (scale bar: 10μm, indicated as $DR5^+$). The H22 cells were transfected with DR5-mCherry plasmid for 24 h, then incubated with BFVs/TRAIL-EGFP (50 μg/mL) for 0.5 h at 4 ℃. The lower panel is the enlarged images of the white dashed box on the upper panel. Related to Figure 3.

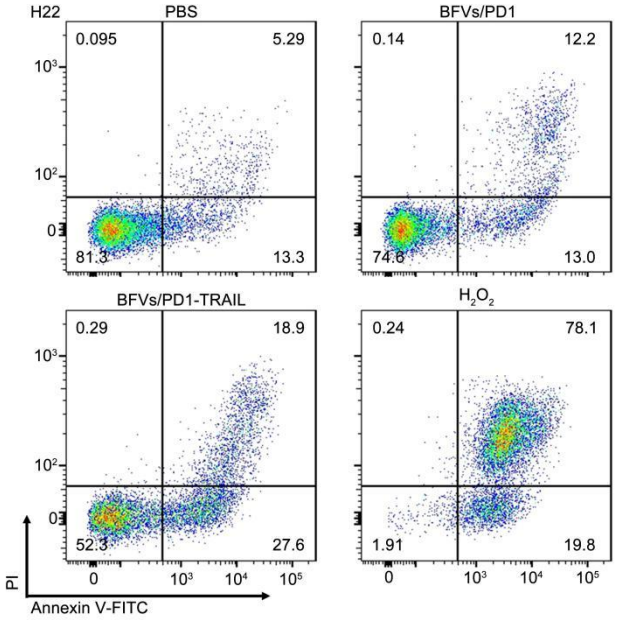

Figure S10. Apoptosis of H22 cells with different treatments by flow cytometry analysis using Annexin V-FITC and PI staining, H_2O_2-treated cells were used as the positive control. Related to Figure 3.

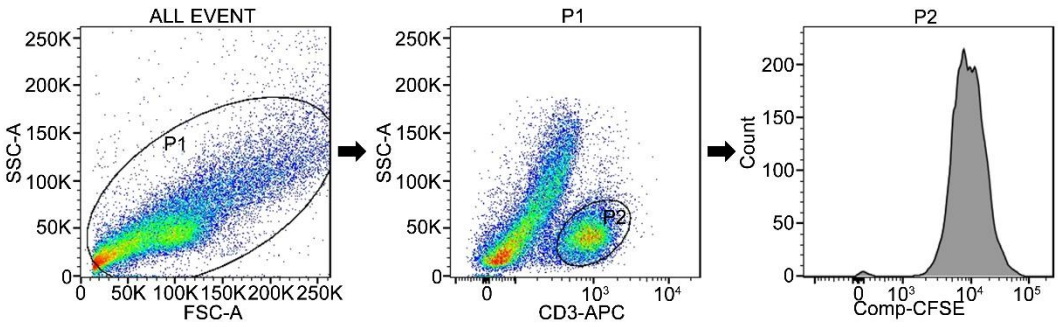

Figure S11. Representative FACS gating strategy for detecting the proliferation of CSFE labeled $CD8^+$ T cells after incubated with the matured DCs. Related to Figure 3.

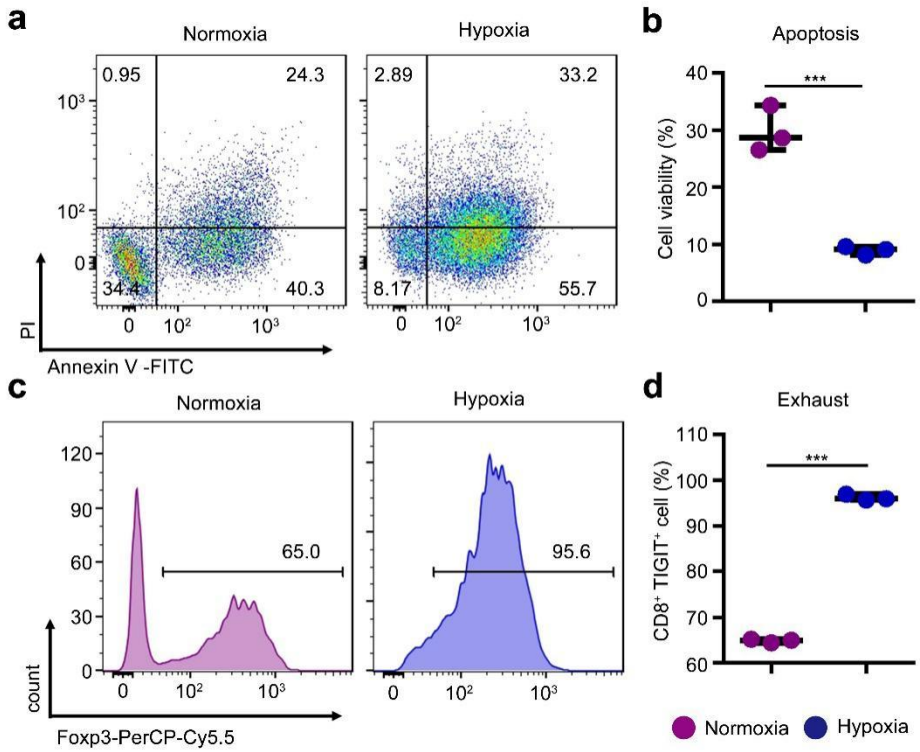

Figure S12. The flow cytometry analysis of the apoptotic state of CTLs under hypoxia or normoxia conditions. (a) The flow cytometry analysis of the apoptosis of CTLs under hypoxia condition or normoxia condition by using Annexin V-FITC and PI staining. (b) The statistical analysis data in a are expressed as min to max, show all points (*P<0.05, **P<0.01, ***P<0.001; n=3). (c) The flow cytometry analysis of the exhaustion of CTLs under hypoxia condition or normoxia condition by using TIGIT-PerCP-eFluor 710 staining. (d) The statistical analysis data in c are expressed as min to max, show all points (*P<0.05, **P<0.01, ***P<0.001; n = 3). Related to Figure 4.

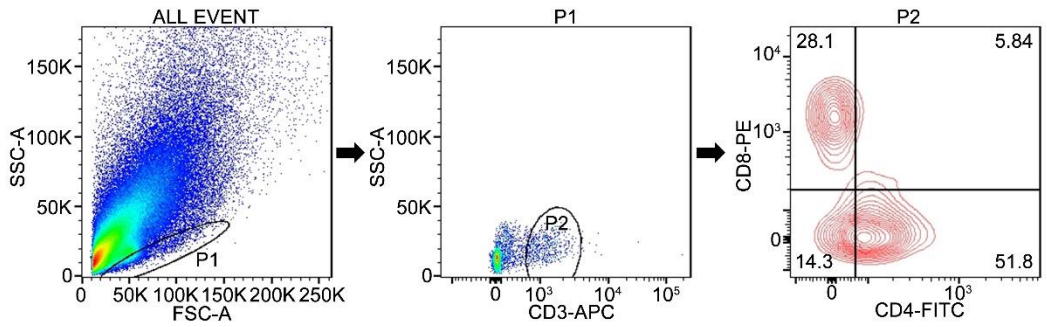

Figure S13. Representative FACS gating strategy for detecting the percentage of $CD4^+$ T cells and $CD8^+$ T cells as indicated in Figure 4h. $CD4^+$ T cells and $CD8^+$ T cells are gated on CD3 positive cells. Related to Figure 4.

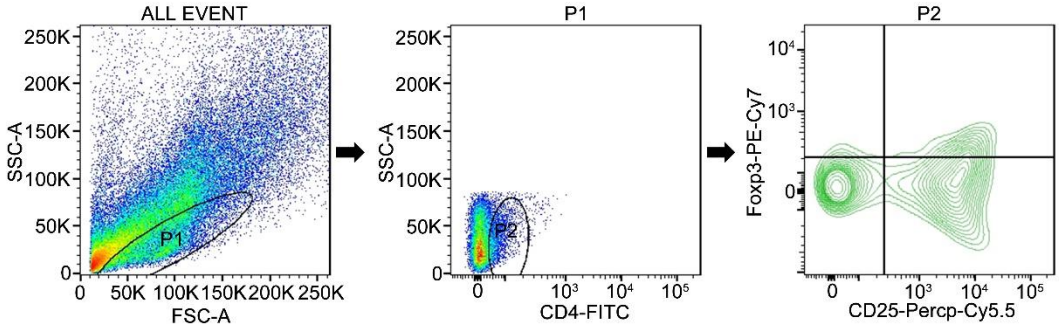

Figure S14. Representative FACS gating strategy for detecting the percentage of Tregs as indicated in Figure 4i. Treg cells ($CD25^+$ $Foxp3^+$) are gated on $CD4^+$ T cells. Related to Figure 4.

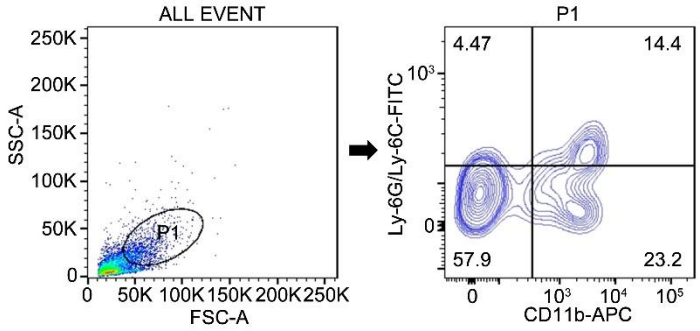

Figure S15. Representative FACS gating strategy for detecting the percentage of MDSCs as indicated in Figure 4j. MDSC are CD11b and Ly-6G/Ly-6C dual positive cells. Related to Figure 4.

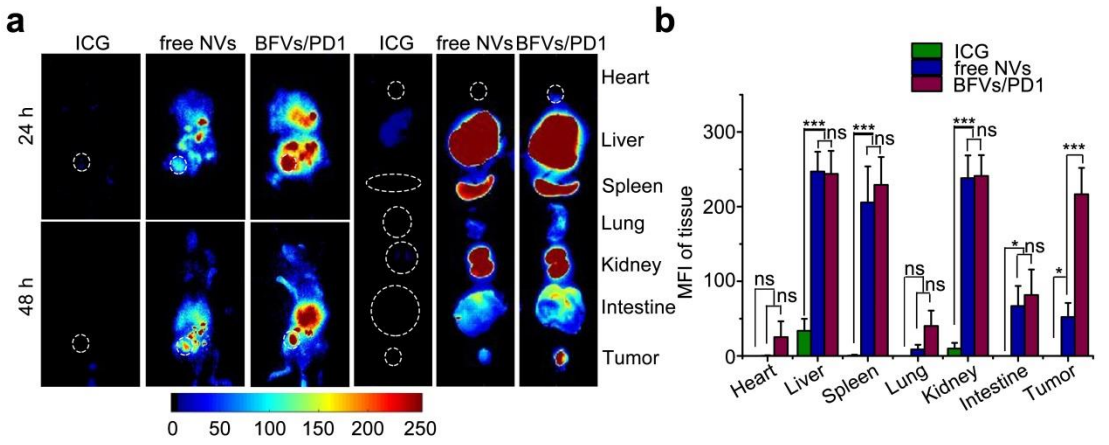

Figure S16. *In vivo* distribution of vesicles in the 4T1 orthotopic murine breast-cancer model. (a) Left panel: *In vivo* fluorescence imaging of the mouse bearing 4T1 tumor at different time points after *i.v.* injection. Right panel: *Ex vivo* fluorescence imaging of major organs and tumor dissected from the mouse after *i.v.* injection of 48 h. (b) The mean fluorescence intensity (MFI) of tumor and major organs. Related to Figure 6.

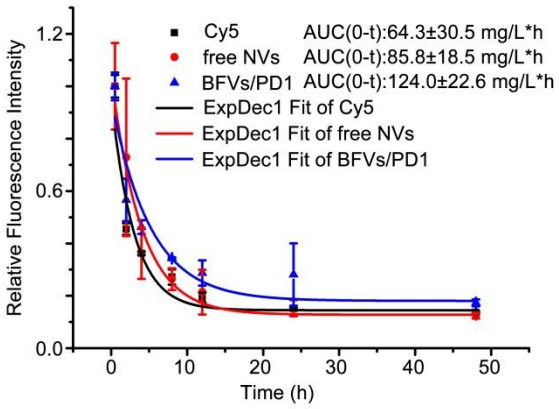

Model	ExpDec1		
Equation	y = A1*exp(-x/t1) + y0		
Reduced Chi-Sqr	13.2352	0.55167	4.21114
Adj. R-Square	0.94372	0.93073	0.92807
		Value	Standard Error
Cy5	y0	0.145	0.01125
	A1	0.81693	0.17837
	t1	2.97315	0.58908
	k	0.33634	0.06664
	tau	2.06083	0.40832
free NVs	y0	0.12791	0.0076
	A1	0.91873	0.13876
	t1	3.95347	0.59572
	k	0.25294	0.03811
	tau	2.74034	0.41292
BFVs/PD1	y0	0.18084	0.02629
	A1	0.77539	0.10761
	t1	5.0995	0.67438
	k	0.1961	0.02593
	tau	3.5347	0.46744

Figure S17. Pharmacokinetics of free Cy5, BFVs/PD1 and free NVs. (a) Relative fluorescence intensity of the serum collected from SD rats with *i.v.* injection of free Cy5, BFVs/PD1(Cy5 labeled, 25 mg/kg based on protein content) or free NVs (Cy5 labeled, 25 mg/kg based on protein content). n=3. Error bar, mean ± s.d. (b) The results of pharmacokinetics were analysis by ExpDec1. The half-life of free Cy5, free NVs and BFVs/PD1 were 3.0 h, 4.0 h and 5.1 h, respectively. The AUC of free Cy5, free NVs and BFVs/PD1 were calculated to be 64.3 ± 30.5 mg/L*h, 85.8 ± 22.6 mg/L*h and 124.0 ± 30.5 mg/L*h respectively. Related to Figure 6.

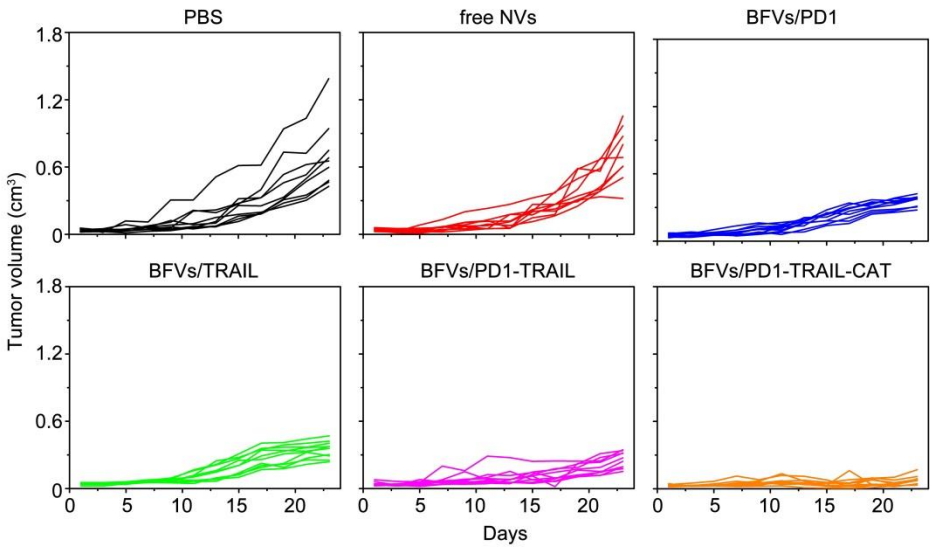

Figure S18. Growth curves for orthotopic tumor on mice after tail vein intravenous injection with PBS, free NVs, BFVs/PD1, BFVs/TRAIL, BFVs/PD1-TRAIL and BFVs/PD1-TRAIL-CAT. Related to Figure 6.

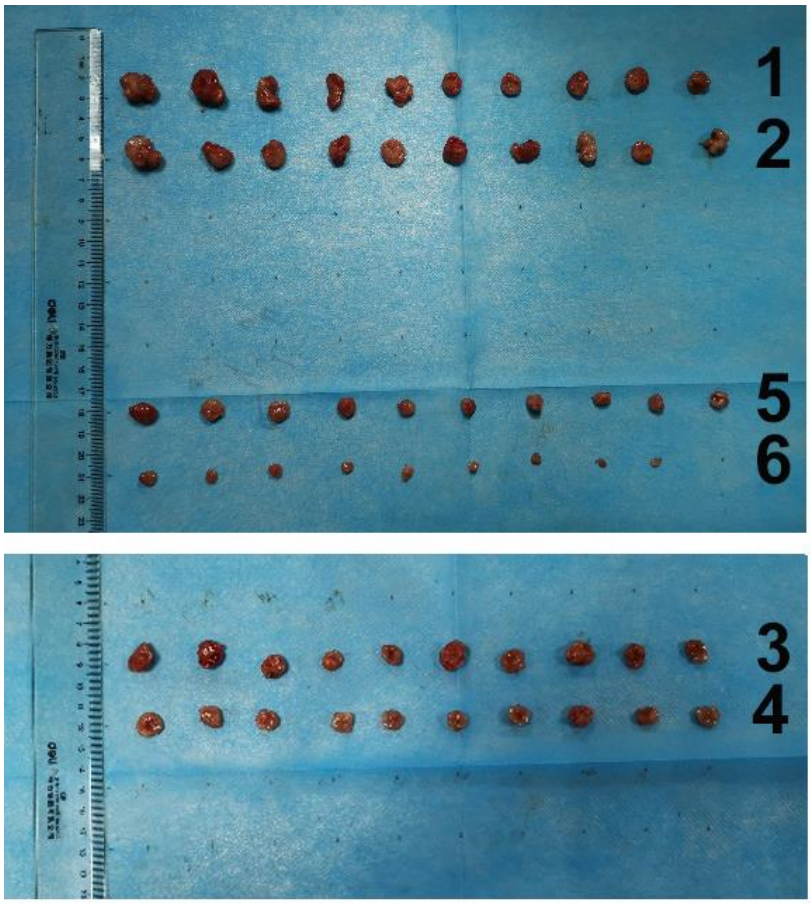

Figure S19. Original photographs of tumor tissues after various treatments in Figure 6d. Related to Figure 6.

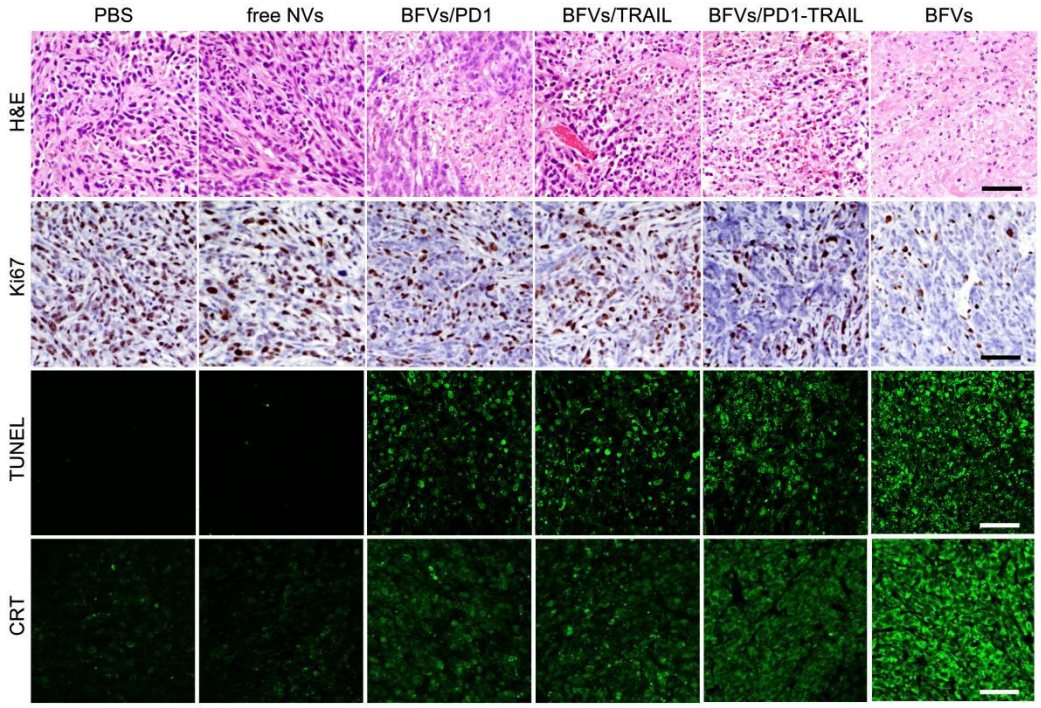

Figure S20. Uncropped images of Figure 6e. Scale bar:50 μm. Related to Figure 6.

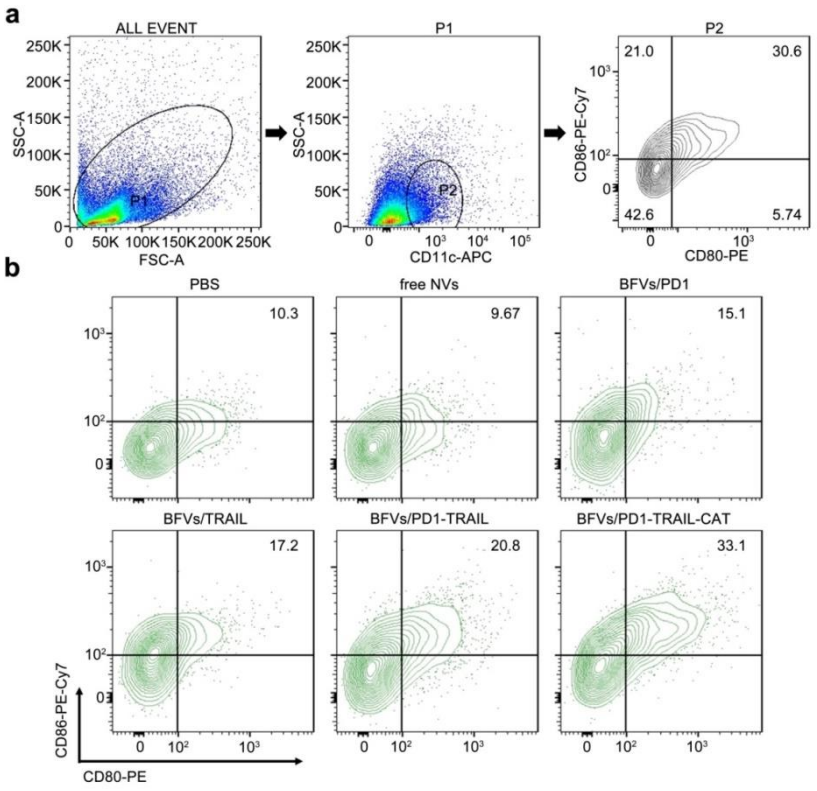

Figure S21. The maturation of DCs (gated on CD11c positive cells) in LNs isolated from the tumor-bearing mice with various treatments by flow cytometry. (a) FACS gating strategy for detecting the maturation of DCs in the LNs. Firstly, we separated the $CD11c^+$ DCs from all cells and then analyzed the CD80 and CD86 in the $CD11c^+$ DCs. (b) The data were acquired by flow cytometry to analyze the maturation of DCs. Related to Figure 6.

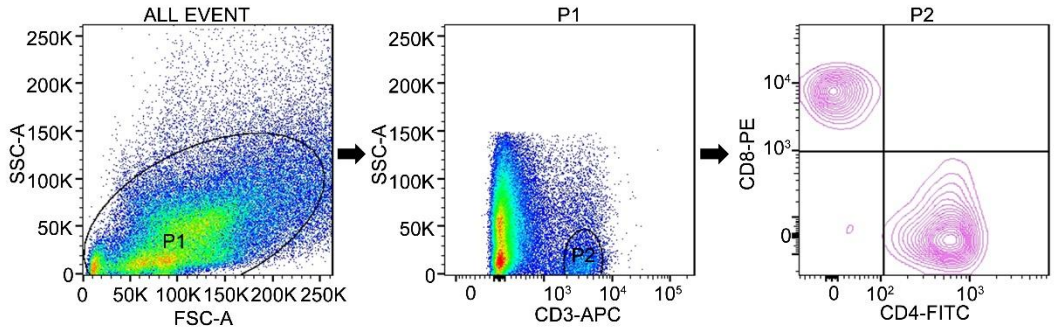

Figure S22. Representative FACS gating strategy for detecting the percentage of $CD4^+$ T cells and $CD8^+$ T cells in the blood. $CD4^+$ and $CD8^+$ are gated on $CD3^+$ T cells. Related to Figure 6.

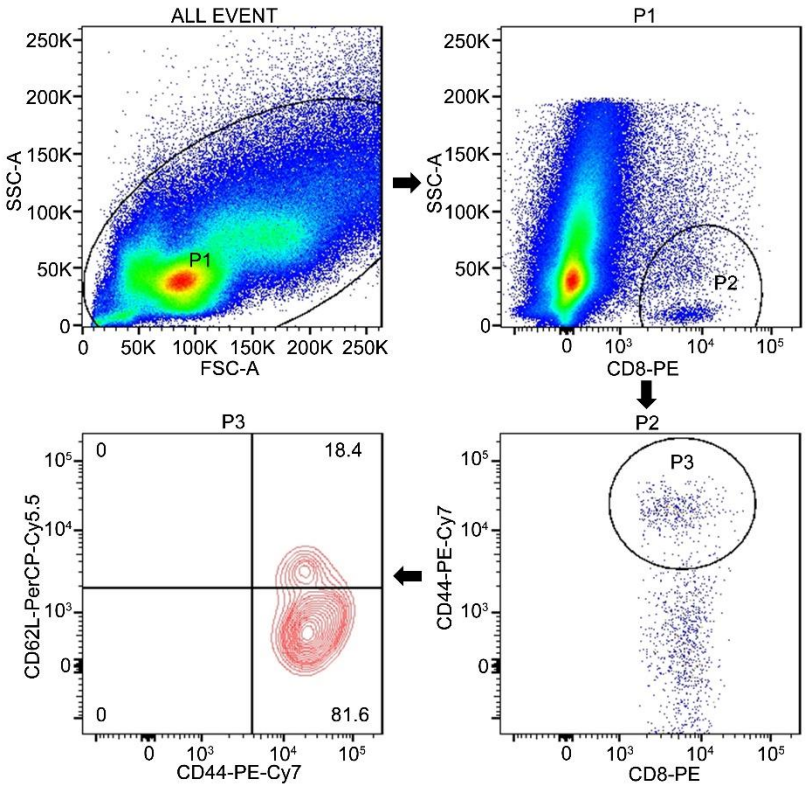

Figure S23. Representative FACS gating strategy for detecting the percentage of $CD8^+$ T_{EM} and $CD8^+$ T_{CM} in the blood. T_{EM} ($CD44^+$ $CD62L^-$) and T_{CM} ($CD44^+$ $CD62L^+$) are gated on $CD8^+$ T cells. Related to Figure 7.

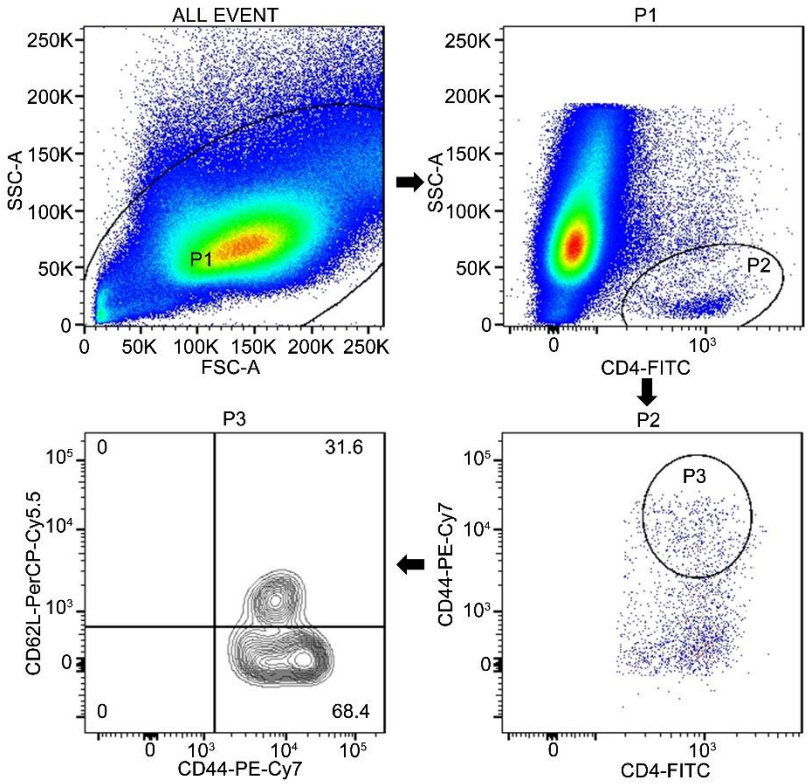

Figure S24. Representative FACS gating strategy for detecting the percentage of $CD4^+$ T_{EM} and $CD4^+$ T_{CM} in the blood. T_{EM} ($CD44^+$ $CD62L^-$) and T_{CM} ($CD44^+$ $CD62L^+$) are gated on $CD4^+$ T cells. Related to Figure 7.

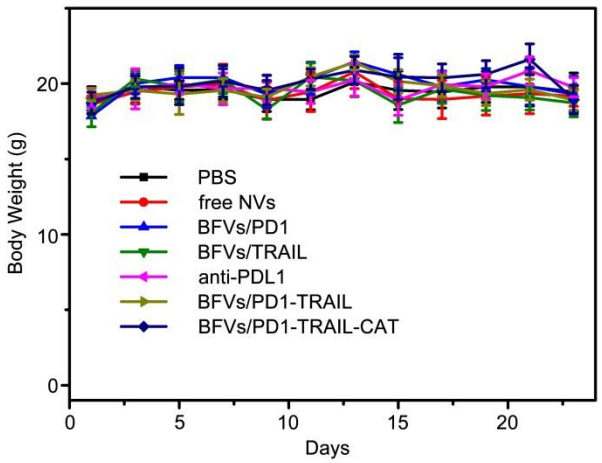

Figure S25. Body weights of the bilateral 4T1 tumor model with indicated treatments. error bar, mean ± s.d (n=8-10). Related to Figure 5.

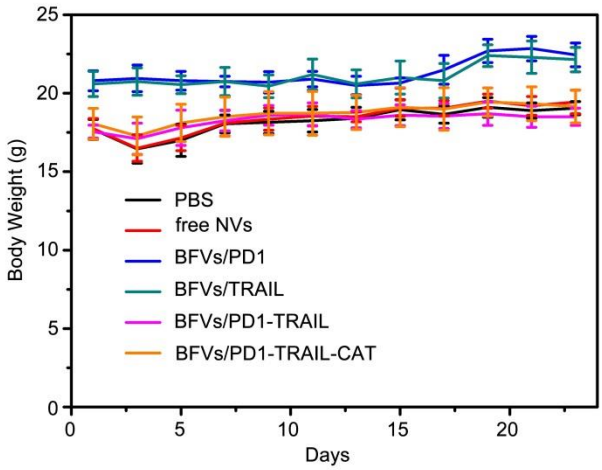

Figure S26. Body weights of the orthotopic 4T1 tumor model with indicated treatments. error bar, mean ± s.d (n=9-10). Related to Figure 6.

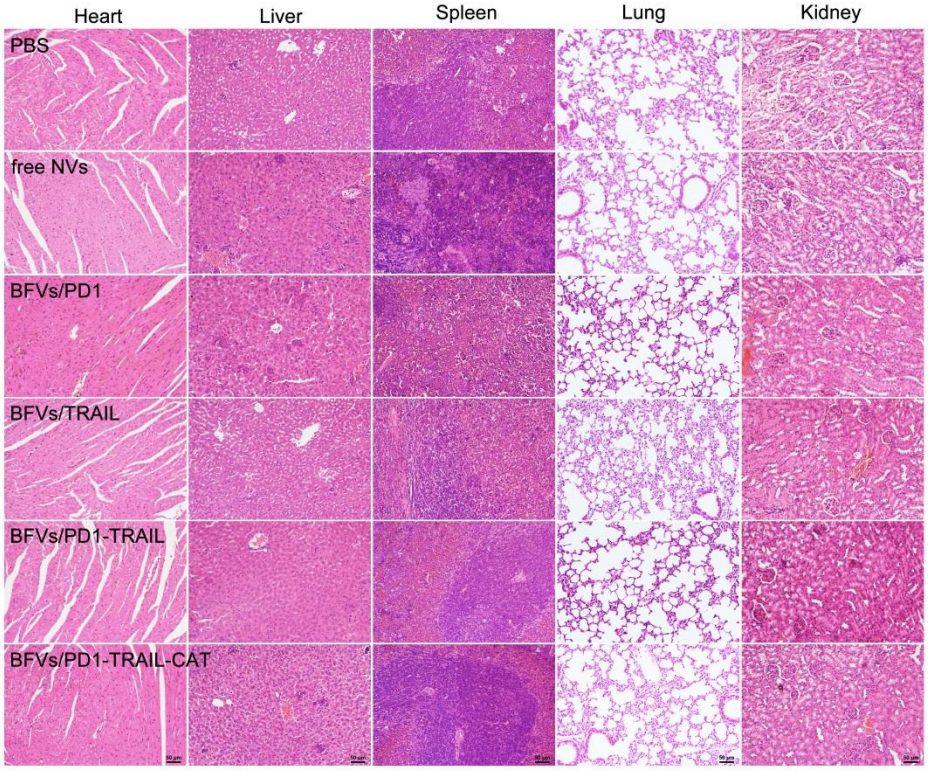

Figure S27. Histological images for H&E staining obtained from the heart, liver, spleen, lung, and kidney of mice with indicated treatments. Tissues were harvested at the day 23 post-injection. Scale bar: 50 μm. Related to Figure 6.

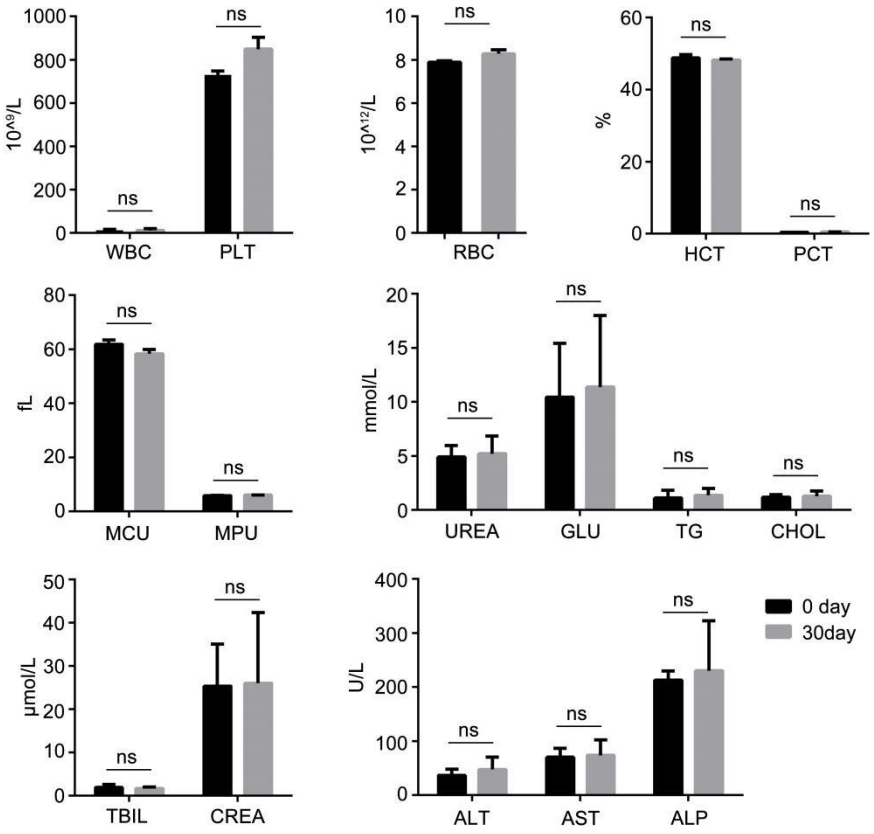

Figure S28. Blood biochemistry analysis of liver and kidney function markers after intravenous injection with PBS and BFVs/PD1-TRAIL-CAT. Date are present as the mean ± s.d (n=3). Related to Figure 6.

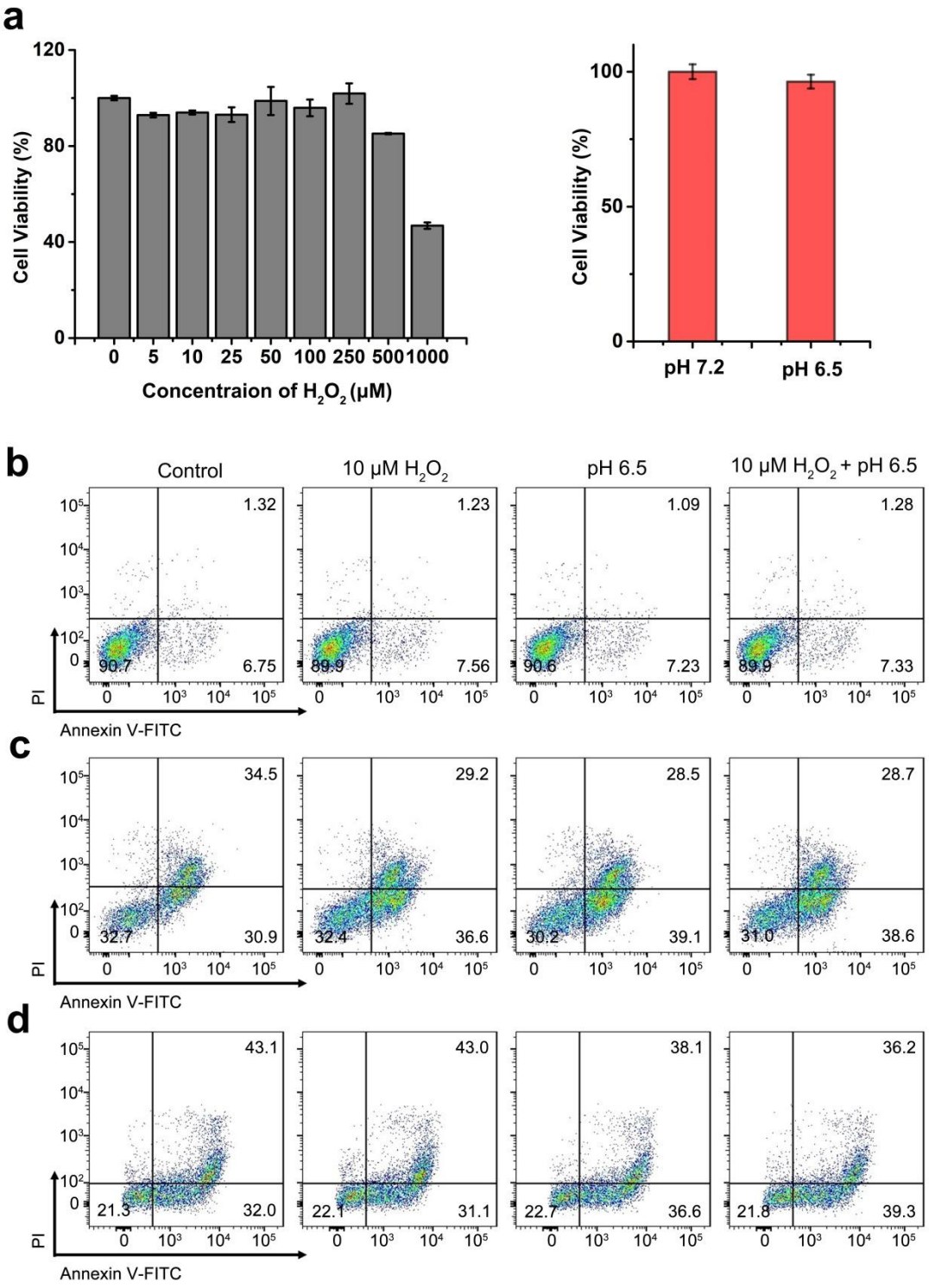

Figure S29. (a) The cell viability of 4T1 cells in different concentration of H_2O_2, or different pH, which was determined by CCK8 assay. (b-d) APCA analysis of the activities of TRAIL and PD1 proteins on BFVs in mimic TME (cell culture medium with 10 μM H_2O_2 at pH 6.5) *in vitro*. (b) 4T1 cells incubated in different culture medium; (c) 4T1 cells incubated with BFVs with membrane presenting TRAIL (BFVs/TRAIL) in different culture medium; (d) 4T1 cells incubated with BFVs with membrane presenting PD1 (BFVs/PD1) in different culture medium for 2 h, and then activated $CD8^+$ T cells were added and incubated for 24 h. Related to Figure 6.

Table S1. $CD8^+$ cell frequency in digested tumor. Related to Figure 4.

Group	A: $CD8^+$ cell frequency in $CD3^+$ (P2 region) (%)	B: Normalization Factor P2 region frequency in ALL EVENTS (FSC/SSC) (%)	C $CD8^+$ cell frequency in ALL EVENTS (%) = A×B
PBS	19.8	2.36	0.47
CAT	21.8	2.9	0.63
BFVs/PD1-TRAIL-CAT	35.3	3.76	1.33

Note: The data in calculation formula is resulted from Figure S12.

Table S2. $CD4^+$ cell frequency in digested tumor. Related to Figure 4.

Group	A: $CD4^+$ cell frequency in $CD3^+$ (P2 region) (%)	B: Normalization Factor P2 region cell frequency in ALL EVENTS (FSC/SSC) (%)	C $CD4^+$ cell frequency in ALL EVENTS (%) = A×B
PBS	57.4	2.36	1.35
CAT	52.4	2.9	1.52
BFVs/PD1-TRAIL-CAT	41.9	3.76	1.58

Note: The data in calculation formula is resulted from Figure S12.

Table S3. Treg cell frequency in digested tumor. Related to Figure 4.

Group	A: $CD25^+$ $Foxp3^+$ cell frequency in $CD4^+$ (P2 region) (%)	B: Normalization Factor P2 region frequency in ALL EVENTS (FSC/SSC) (%)	C $CD4^+$ $CD25^+$ $Foxp3^+$ cell Frequency in ALL EVENTS (%) = A×B
PBS	27.7	4.41	1.22
CAT	15.8	4.54	0.72
BFVs/PD1-TRAIL-CAT	11.3	5.51	0.62

Note: The data in calculation formula is resulted from Figure S13.

Table S4. MDSC cell frequency in digested tumor. Related to Figure 4.

Group	A: $CD11b^+$ $Ly\text{-}6G/Ly\text{-}6C^+$ cell frequency in P1 region (%)	B: Normalization Factor P1 region cell frequency in ALL EVENTS (FSC/SSC) (%)	C $CD11b^+$ $Ly\text{-}6G/Ly\text{-}6C^+$ cell frequency in ALL EVENTS (%) = A×B
PBS	29.0	18.5	5.37
CAT	17.6	19.7	3.47
BFVs/PD1-TRAIL-CAT	10.1	18.1	1.83

Note: The data in calculation formula is resulted from Figure S14.

Transparent Methods

Establishment of genetically engineered stable cell lines

First, we constructed the plasmids which encoded murine PD1 with mCherry-tag fused at the C-terminal region (pcdh-CMV-PD1-mCherry-puro) and murine TRAIL with EGFP-tag fused at the C-terminal region (pcdh-CMV-EGFP-EGFP-blastcidin). Lentivirus were produced by using HEK 293FT cells with Lipofectamine 3000 Transfection Kit (Thermo Fisher Scientific, lot:2098843) and concentrated by ultracentrifugation at 25, 000 rpm for 90 min at 4 ℃. Then, the HEK 293FT cells were infected with the lentivirus and incubated with 5 μg/mL polybrene (Santa Cruz biotechnology, sc-134220). Two days after infection, the 293FT cells were cultured in DMEM with 10% FBS and screened with puromycin (5 μg/mL) or blastcidin (10 μg/mL) to select cells stably expressing murine PD1 or TRAIL for a week. Finally, the PD1-mCherry stable expressing HEK 293FT cells or TRAIL-EGFP stable expressing HEK 293FT cells were cultured in DMEM medium with 10% FBS.

Preparation of biosynthetic functional vesicles (BFVs)

PD1-mCherry stable expressing HEK 293FT cells and TRAIL-EGFP stable expressing HEK 293FT cells were cultured in DMEM medium with 10% FBS. For

collecting cell membrane, the cells were harvested with trypsin and washed with PBS for 2 times by centrifugation with 300×g for 5 min. Then, the Membrane and Cytosol Protein Extraction Kit (Beyotime, P0033) was used to extract the cell membrane. Afterwards, the cell membrane was washed with PBS containing PMSF and protease inhibitor cocktail for 3 times. To prepare biosynthetic functional vesicles (BFVs), the cell membrane and catalase (CAT) protein in PBS buffer were evenly mixed (mass ratio=1:1, based on protein weight) and then passed through 1 μm filter for 11 times. The entire solution was centrifuged at 13,000×g for 30 min at 4 ℃, and the obtained sediment was washed with PBS buffer for 3 times, followed by successively passed through 0.4 μm,0.2 μm and 0.1 μm pore-sized polycarbonate membrane filters for another 11 times. The vesicles were then purified by Sephadex G-75 column to obtain the final product of BFVs.

To determine the specific ratio and content of TRAIL, PD1 and CAT, Cy5-NHS labeled CAT was used to prepare the final product of BFVs according to above method. After lysis by the Solution B supplied in the Membrane and Cytosol Protein Extraction Kit (Beyotime, P0033), the BFV lysates were divided into four equal parts. One part was quantified by the Easy II Protein Quantitative Kit (BCA, TransGen Biotech, DQ111-01) to determine the total protein content; one part was used to determine the CAT content by fluorescence measurement according to the established concentration-emission correlation curve of Cy5 labeled CAT; the residual two parts were determined by ELISA to respectively analyze the TRIAL and PD1 content (R&D SYSTEMS, DY1121 for TRAIL and DY1021 for PD1).

Western blot

Immunoblotting analysis was used to characterize the stable expression of PD1-mCherry and TRAIL-EGFP in HEK 293FT cells. Briefly, the stable expression

cells and the parent HEK 293FT cells were lysed with RIPA buffer for 30 min on ice. Then, the supernatant was collected after centrifugation at 10,000×g for 30 min at 4 ℃. The protein concentration was quantified by the Easy II Protein Quantitative Kit (BCA, TransGen Biotech, DQ111-01), and the loading buffer was added equally into the supernatant before heated to 100℃ for 10 min. Then 10% SDS-PAGE was used to separate the samples that were further analyzed by immunoblotting using the primary antibody of PD1 (1 μg/mL, abcam, ab214421), TRAIL (1 μg/mL, abcam, ab10516) and the corresponding secondary antibodies, and finally revealed by SuperSignal™ West Pico PLUS Chemiluminescent Substrate and recorded by the ChemiDoc™ MP imaging system.

Immunoprecipitation (IP) assay

To verify the right outside-out orientation of PD1 on the biosynthetic functional vesicles, the IP assays were performed. Briefly, the vesicles with surface presenting PD1 (termed as BFVs/PD1) were dispersed in 1 mL ice-cold PBS, and then incubated with 100 μL of 50% protein A/G agarose beads for 2 h at 4 ℃ with gentle rotation. Afterwards, the above mixture underwent centrifugation at 10,000 rpm for 15 min at 4 ℃ to precipitate the protein A/G agarose beads that were nonspecifically bond with BFVs/PD1. Then, the supernatant containing BFVs/PD1 was incubated with PD1 primary antibody (10 μg/mL, abcam, ab214421) and protein A/G agarose beads in the rotation condition overnight at 4 ℃. Afterwards, the beads were washed gently with ice-cold PBS for 3 times. Finally, the samples were subjected to 10% SDS-PAGE and analyzed by western blot using the relevant antibodies. Meanwhile, the group that used IgG to substitute PD1 primary antibody was used as the control.

Cell binding assay

The 4T1 cells were cultured in the confocal dishes overnight, then BFVs/PD1 or free NVs labeled with FITC (50 μg/mL based on protein content) were added to the medium and incubated for another 4 h at 37 ℃. Meanwhile, the cells that were pretreated with anti-PDL1 antibody (10 μg/mL, abcam, ab213480) for 2 h before the addition of BFVs/PD1 were selected as the competition control group. Afterwards, the cells were washed with PBS, fixed with 4% paraformaldehyde for 15 min and stained with DAPI for 10 min. Finally, the cells were washed with PBS for 3 times before observed by CLSM (Zeiss LSM780).

Protein co-localization assay

The 4T1 cells or H22 cells were cultured in the confocal dishes overnight, then these cells were transfected with PDL1-EGFP plasmid for 24 h, followed by the incubation with BFVs/PD1 (50 μg/mL based on protein content) for 30 min at 4 ℃. Then, the cells were imaged by CLSM as mentioned above. Similarly, the co-localization assay between TRAIL on vesicles and DR5 on cancer cells was carried out through the same protocol.

Isolation of $CD8^+$ T cells from mouse spleen

$CD8^+$ T cells were isolated from mouse spleen according to the following method. In brief, the spleen was harvested from 8 week old Balb/c mice and kept in RPMI 1640 medium on ice. Then, the cells were flushed out from spleen by RPMI 1640 culture medium through a syringe. The medium containing cells was passed through 40 μm cell strainer to remove the large debris. Afterwards, the cells were collected by centrifugation at 800×g for 5 min, followed by suspended in red blood cell lysis buffer for 10 min at room temperature to lyse red blood cells. Subsequently, the cells were washed with RPMI 1640 medium by centrifuging 5 min at 800×g. Then, the

$CD8^+$ T cells were sorted through CD8 (TIL) MicroBeads (Miltenyi Biotec, 130-116-478) according to the manufacturer's instructions. The $CD8^+$ T cells were seeded in a 6-well plate with KBM 581 medium and supplemented with IL-2 (10 ng/mL, R&D systems, MX2918061), anti-CD3ε antibody (5 μg/mL, biolegend, 100331) and anti-CD28 antibody (2 μg/mL, biolegend, 102112) to activate the $CD8^+$ T cells. The activated $CD8^+$ T cells were cultured for 5 days before seeded in 6-well plate for further use.

CTL cytotoxicity assay

The 4T1 cells in 6-well plate were incubated with free NVs (50 μg/mL based on protein content), BFVs/PD1 (50 μg/mL based on protein content) or anti-PDL1 antibody (10 μg/mL) for 2 h, then the activated CTLs ($CD8^+$ T cells) were added into 4T1 cells (CTLs:4T1 = 1:1, number ratio). After 24 h of co-incubation, the culture medium was collected for determining Granzyme B by using Mouse Granzyme B ELISA Kit (Boster, EK1115), while the cells were stained with Annexin V-FITC/PI (DOJINDO Laboratories, NX610) and anti-CD3-APC antibody (Thermo Fisher Scientific eBioscience™, 12-0081-82). Finally, the cells were washed with PBS for 3 times and detected by flow cytometry (BD, FACSVerse, USA). PDL1overexpression 4T1 cells with PBS treatment were used as the negative control.

CRT expression on cancer cells after different treatment

The 4T1 cells in the confocal dishes were incubated with BFVs/PD1 or BFVs/PD1-TRAIL, and the cells treated with PBS were taken as control. After 24 h of incubation, the cells were washed with PBS, fixed with 4% paraformaldehyde for 15 min, and then stained with the primary antibody of CRT (5 μg/mL, abcam, ab2908) for 2 h and the corresponding secondary antibody for 1 h at room temperature. Then,

the cells were washed with PBS and stained with Hoechst for 10 min. Finally, the cells were observed by CLSM (Zeiss LSM780).

Isolation of DC cells from mouse bone marrow

DC cells were isolated from bone marrow according to the following method. Firstly, the tibias and femurs were isolated from 8 week old Balb/c mice and kept in RPMI 1640 medium on ice. The end of each bone was cut off with scissors, and then the cells were flushed out from bone by RPMI 1640 culture medium through a syringe. The medium containing cells was passed through 40 μm cell strainer to remove the large debris. Then, the cells were collected by centrifugation at 800×g for 5 min, followed by suspended in red blood cell lysis buffer for 10 min at room temperature to lyse red blood cells. Subsequently, the cells were washed with RPMI 1640 medium through centrifuging 5 min at 800×g, then seeded in a 6-well plate with RPMI 1640 medium and cultured with mouse granulocyte/macrophage colony stimulating factor (mGM-CSF, 20 ng/mL, R&D systems, 415-ML-020/CF) and IL-4 (10 ng/mL, 404-ML-010/CF) for 3-5 day to induce DC differentiation for further usage.

DCs maturation assay

The 4T1 cells were treated with BFVs/PD1 or BFVs/PD1-TRAIL for 24 h, and then the supernatant was transferred into a new 24-well plate with DCs for triggering their maturation. The DCs treated with LPS was used as the positive control. After 48 h of incubation, the culture medium was collected for cytokine detection by using Mouse ELISA Kit (TNFα, Boster, EK0527; IFNγ, Boster, EK0375; IL12-P70, Boster, EK0422), while the cells were stained with the antibody of CD11c-APC (eBioscience™, 17-0114-82), CD80-PE (eBioscience™, 12-0801-82) and

CD86-PE-Cy7 (eBioscience™, 25-0862-82). Finally, the cells were washed with PBS for 3 times and detected by flow cytometry.

Measurement of O_2 production

The oxygen concentration in aqueous solution was measured using a portable dissolved oxygen meter (Rex, JPBJ-608, China). For measurement of BFVs to generate O_2, the BFVs (10 μg/mL based on protein content) were added into H_2O_2 (0.5 mM) aqueous solution, and then the oxygen electrode probe was inserted into the tube to measure the oxygen concentration of the solution in real time.

Intracellular H_2O_2 and O_2 detection

Hydrogen peroxide assay Kit (Cell-based, abcam, ab138874) and $[Ru(dpp)_3]Cl_2$ probe were used to detected the intracellular H_2O_2 and oxygen levels, respectively. In detail, the 4T1 cells were seeded into a 96-well plate and incubated in hypoxia container. After 24 h of incubation, the BFVs/PD1-TRAIL or BFVs/PD1-TRAIL-CAT were added into 96-well and further incubated for 2 h. After being washed twice with PBS, the intracellular H_2O_2 and O_2 were detected according to the manufacturer's instructions and observed by a fluorescence microscope (Zeiss Axio Vert.A1, Germany).

Antitumor evaluation on bilateral 4T1 tumor model

The Balb/c mice were purchased from China Wushi, Inc. (Shanghai, China). All animal experiments were approved by the Animal Ethics Committee of Mengchao Hepatobiliary Hospital of Fujian Medical University and were carried out according to the institutional guidelines. For establishing this model, the left side of each mouse was subcutaneously (*s.c.*) injected with 1×10^6 4T1 cells and the right side was *s.c.* injected with 5×10^5 4T1 cells. When the volume of left side tumor reached about 100

mm^3 while the right side tumor volume reached about 50 mm^3, the tumor-bearing mice were randomly divided into 7 groups for subsequent experiment. Each tumor-bearing mice was intratumorally (*i.t.*) injected in the left side of the tumor with PBS, free NVs (5 mg/kg based on protein content), BFVs/PD1 (5 mg/kg based on protein content), BFVs/TRAIL (5 mg/kg based on protein content), anti-PDL1 antibody (0.4 mg/kg, biolegend, 124328), BFVs/PD1-TRAIL (5 mg/kg based on protein content) and BFVs/PD1-TRAIL-CAT (5 mg/kg based on protein content) for a total of 4 times in every 3 days. The tumors were measured by using a vernier calipers and the volume (V) was calculated to be $V=a\times b^2/2$, where a is the longest and b is shortest diameter of the tumor, respectively. To assess potential toxicities, mice were monitored for weight change. Mice were sacrificed when exhibited signs of impaired health or when the tumor volume exceeded 1200 cm^3.

Pharmacokinetics of vesicles

PD1 presenting vesicles (BFVs/PD1) and blank vesicles (free NVs) labeled with Cy5-NHS were *i.v.* injected in SD rats *via* tail-vein in 200 μL of final volume at a dose of 25 mg/kg based on protein content. Peripheral blood was collected at different time points after injection, and the fluorescence of the serum was measured.

***In vivo* distribution of BFVs**

The 4T1 orthotopic murine breast-cancer model was established by injection of 4T1 cells (5×10^5) into the mammary fat pads of mice on the abdomen to investigate the *in vivo* distribution of BFVs labeled with ICG-NHS after intravenous (*i.v.*) injection. At different time post-injection, the whole body fluorescence images were acquired by NIR II fluorescence imaging system (UNITED WELL). After 48 h of injection, the

mice were euthanized, and the tumor and other major organs including heart, liver, spleen, lung, kidney, and intestine were dissected and imaged.

In addition to the histopathological observation of major organs, we also evaluated the toxicity of BFVs by blood routine and serum biochemistry analysis. After treatment, the blood of SD rats was collected in EDTA2K spray-coated tubes and analyzed using an automated hematology analyzer in one go.

Antitumor evaluation on orthotopic 4T1 tumor model

When the volume of tumor reached about 50 mm^3, the mice were randomly divided into 6 groups for the following treatments. PBS, free NVs (25 mg/kg based on protein content), BFVs/PD1 (25 mg/kg based on protein content), BFVs/TRAIL (25 mg/kg based on protein content), BFVs/PD1-TRAIL (25 mg/kg based on protein content) and BFVs/PD1-TRAIL-CAT (25 mg/kg based on protein content) were administered into tumor-bearing mice by tail-vein injection. The tumor size was measured as mentioned above. The tumor and major organs (heart, liver, spleen, lung and kidney) were harvested at the end of antitumor studies, fixed in 4% formalin solution, dehydrated, deparaffinization and subjected to H&E staining, Ki67 immunohistochemical and other immunofluorescence staining analysis.

Immune memory effect for inhibiting tumor lung metastasis

The orthotopic 4T1 tumor-bearing mice underwent the aforementioned treatments. At the day 23, the residual tumor was surgically removed from the mice and then the wound was closed. One week later, 5×10^5 4T1 cells were injected into the mice through caudal vein. After 2 weeks, the lungs were isolated from treated mice to photograph and count the metastasis nodules, and further fixed in 4% formalin solution for H&E staining.

Intra-tumoral H_2O_2 concentration detection

The tumor bearing Balb/c mice were respectively *i.t.* injected with 100 μL of PBS, CAT (5 mg/kg) or BFVs/PD1-TRAIL-CAT (CAT, 5 mg/kg). After injection for 4 h, the tumors isolated from euthanized mice were weighted and homogenized with 800 μL cold acetone by automatic sample rapid grinding machine. Then, the supernatant was collected by centrifugation at 13,000 rpm for 10 min. Subsequently, 10 μL of $TiOSO_4$ (0.03 M) and 20 μL of $NH_3 \cdot H_2O$ were added into the supernatant and the sediments were immediately collected by centrifugation at 13000 rpm for 10 min. Finally, the sediments were dispersed in 300 μL of H_2SO_4 (1mM) to measure the absorbance at 405 nm by using the Spectra Max M5 microplate reader (Molecular Devices, USA). The final result of intra-tumoral H_2O_2 concentration was calculated according to the standard curve.

Intra-tumoral O_2 detection

To determine whether the BFVs can alleviate hypoxia in tumor, the tumor bearing Balb/c mice were established and treated with PBS, CAT or BFVs/PD1-TRAIL-CAT (5 mg/kg based on protein content) by *i.t.* injection. The photoacoustic images at different time points were acquired to evaluate the dissolved oxygen status of the tumor site by small animal ultrasonic imaging system (VisualSonic Vevo 3100 LAZR system, Canada). We further confirmed this result by immunohistochemistry of tumor slices as follows. After two days of injection, the mice were administrated with a hypoxia probe Hypoxyprobe^{TM}-1(1.5 mg/mouse) by intraperitoneal injection, then the tumors were harvested after 1 h. The harvested tumors were sliced and

immune-stained with FITC-MAb antibody (5 μg/mL) for CLSM observation. The hypoxia probe and antibody were from Hypoxyprobe^{TM} Green Kit (Hypoxyprobe,Inc, HP6-100 Kit, USA).

Immune response analysis *in vivo*

To examine DC maturation *in vivo*, 4T1-tumor bearing mice were treated with various formulation of vesicles as indicated. Then, the draining inguinal lymph nodes were isolated after 3 days of treatment. The cells were harvested from lymph nodes by gently grinding and then examined by flow cytometry after staining with CD11c-APC (eBioscience™, 17-0114-82), CD80-PE (eBioscience™, 12-0801-82) and CD86-PE-Cy7 (eBioscience™, 25-0862-82).

To examine the infiltration of CTLs, MDSCs, Tregs in tumor, the 4T1-tumor bearing mice were treated with indicated conditions. Then, the tumors were isolated after 3 days of treatment. Subsequently, the tumors were digested in RPMI 1640 by collagenase type IV (1 mg/mL), hyaluronidase (0.2 mg/mL), deoxynbonuclease I (0.02 mg/mL) for 1 h at 37 ℃. Then, the medium containing cells were passed through 40 μm cell strainer to remove the large debris, the cells were collected by centrifugation at 800×g for 5 min, and further purified by a density gradient centrifugation by 30% percoll separating solution at 800×g for 30 min at 4 ℃. Afterwards, the cells were harvested and then examined by flow cytometry after stained with anti-CD3-APC (eBioscience™, 17-0032-82), anti-CD4-FITC (eBioscience™, 11-0042-85) and anti-CD8-PE (eBioscience™, 12-0081-82) antibodies for CTLs, anti-CD4-FITC (eBioscience™, 11-0042-85), anti-CD25-PerCP-Cy5.5 (eBioscience™, 46-0251-82) and anti-Foxp3-PE-Cy7 (eBioscience™, 25-5773-80) antibodies for Tregs, anti-CD11b-APC (eBioscience™,

17-0112-82) and anti-Ly-6G/Ly-6C-PE(eBioscience™, 12-5931-82) antibodies for MDSCs.

To examine the memory T cells, the blood collected from the treated mice was diluted with PBS (blood volume:PBS volume = 1:1) and subject to a density gradient centrifugation in Ficoll-Paque^{TM} PREMIUM sterile solution at 800 × g for 30 min at 4 ℃. The cells were harvested and then examined by flow cytometry after staining with anti-CD4-FITC (eBioscience™, 11-0042-85), anti-CD44-PE-Cy7 (eBioscience™, 25-0441-82) and anti-CD62L-PerCP-Cy5.5 (eBioscience™, 45-0621-82) antibody or anti-CD8-PE (eBioscience™, 12-0081-82), anti-CD44-PE-Cy7 (eBioscience™, 25-0441-82) and anti-CD62L-PerCP-Cy5.5 (eBioscience™, 45-0621-82) antibody.

Intracellular cytokine assay

To examine the produced cytokines in tumor, the tumors isolated from sacrificed mice were weighted and homogenized with 1 mL PBS (1mL PBS per 50 mg tumor) containing PMSF and protease inhibitor cocktail. Then the supernatants were collected by centrifugation at 10, 000 rpm for 10 min. Subsequently, the collected supernatant was used for cytokine detection by using Mouse ELISA Kit (TNFα, Boster, EK0527; IFNγ, Boster, EK0375; IL-12, Boster, EK0422; Granzyme B, Boster, EK0417; IL-10, Boster, EK1115; TGF β, Boster, EK0515).

Statistical analysis

All results are presented as the mean ± s.d. or min to max with show all points as indicated. Significance among different groups was calculated using One-way ANOVE (and nonparametric) with post-hoc tests. Survival rate in different groups

was compared using a Log-Rank test. All statistical analyses were carried out by GraphPad Prism 6.01. The P-value < 0.05 was considered as statistically significant.